NANO · MICRO small
www.small-journal.com

IL-21 Loading $CaMnCO_3$ Vitality Backpacks Boost CAR-T Cell Synergistic Immunotherapy

Baihui Wang, Yuchan Xue, Yang Jia, Yuyao Duan, Dejun Li, Minghao Sui, Yuemin Feng, Le Wang, Han Ding, Xinyu Wang, Tianru Zhang, Yanning Sun, Huimin Liu, Jianni Qi, Jiazhi Duan, Songbo Zhao,* and Qiang Zhu**

Chimeric antigen receptor (CAR)-T-cell therapy achieves considerable success in the treatment of malignant tumors, but clinical relapse due to the tumor microenvironment (TME) is very common. The TME of solid tumors is characterized by weak acidity, hypoxia, and elevated reactive oxygen species (ROS) levels, which collectively impair the function and persistence of infiltrating CAR-T cells. In this study, acid-sensitive responsive $CaMnCO_3$ nanoparticles (CMC NPs), are developed that simultaneously mitigate TME acidosis and hypoxia. IL-21 is encapsulated within CMC NPs (denoted as CMC-21), which are then surface-conjugated to CAR-T cells as functional 'vitality backpacks' to enhance cellular activity. The CMC-21 backpack enables sustained release of IL-21, persistently enhancing CAR-T cell antitumor immunity across both low- and high-dose infusion regimens. Furthermore, CMC NPs exert dual modulatory effects on the TME by: 1) consuming protons to neutralize acidic conditions, and 2) catalytically converting endogenous H_2O_2 to O_2 to relieve hypoxia. This multimodal remodeling of the immunosuppressive TME significantly enhances the infiltration and activity of adoptively transferred CAR-T cells while simultaneously boosting endogenous T cell and NK cell recruitment in vivo. These findings establish a novel CAR-T cell enhancement strategy through sustained IL-21 release from CMC-21 backpacks, offering new possibilities for solid tumor immunotherapy.

1. Introduction

Chimeric antigen receptor T (CAR-T) cell therapy is a revolutionary technology that has achieved remarkable success in treating hematological malignancies. Despite the potential benefits of CAR-T cell immunotherapy, challenges associated with its safety and efficiency remain.[1] Limited efficacy against solid tumors and limited persistence caused by exhaustion, poor trafficking, and tumor infiltration are the major limitations of CAR-T cell therapy. Compared with those of hematological malignancies, the characteristics of solid tumors, especially hepatocellular carcinoma (HCC), including antigen heterogeneity, an immunosuppressive tumor microenvironment (TME), and a thick extracellular matrix, render CAR-T cell therapy less efficient.[2,3] The TME of solid tumors is characterized by abnormal tumor cell proliferation and tumor vascularization, which ultimately lead to hypoxia, low pH, overexpressed glutathione (GSH), and high levels of H_2O_2 in tumor metabolomics.[4–8] Simultaneously, the TME releases multiple immunosuppressive signals, including immunosuppressive cells and cytokines, which limit the effectiveness of immunotherapy.[9] In addition, many immunosuppressive cells in the TME, including myeloid-derived suppressor cells, regulatory T cells, and tumor-associated macrophages, can infiltrate solid tumors, driving the production of suppressor cytokines, chemokines, and growth factors. These factors hinder the

B. Wang, Y. Xue, M. Sui, Y. Feng, L. Wang, H. Ding, X. Wang, T. Zhang
Department of Gastroenterology
Shandong Provincial Hospital Affiliated to Shandong First Medical University
Jinan, Shandong 250021, P. R. China

The ORCID identification number(s) for the author(s) of this article can be found under https://doi.org/10.1002/smll.202501645

DOI: 10.1002/smll.202501645

B. Wang
Department of Gastroenterology
Qilu Hospital (Qingdao)
Cheeloo College of Medicine
Shandong University
Qingdao, Shandong 266001, P. R. China

Y. Jia
Department of Thoracic Surgery
Shandong Provincial Hospital affiliated to Shandong First Medical University
Jinan, Shandong 250021, P. R. China

Y. Duan
Reproductive Medical Center
The Second Affiliated Hospital of Shandong University of Traditional Chinese Medicine
Jinan, Shandong 250012, P. R. China

infiltration, survival, and antitumor activity of CAR-T cells in solid tumors, making the TME a serious challenge in CAR T-cell synergy therapy.[10] Therefore, effective strategies that reshape the TME and improve CAR-T cell therapy are urgently needed.

Interleukin 21 (IL-21) has been widely studied owing to its strong potential in the application of tumor biotherapy.[11] IL-21 is an immunomodulatory protein that regulates the immune response by affecting various immune cells. IL-21 exerts multiple effects on T-cells, including enhancing their cell proliferation, cytotoxic effects, persistence, and function, as well as preventing functional exhaustion, all of which improve T-cell tumor-killing ability. In tumor therapy, IL-21 has lower toxicity than that of IL-2 and has shown enhanced antitumor ability against solid cancers in both preclinical and clinical studies.[12] In the TME, IL-21 exhibits significantly lower cytotoxicity than dose IL-2 while exerting superior cell-killing effects.[13] However, IL-21 plays a limited role in antitumor treatments because of its short half-life. Therefore, an effective platform loaded with IL-21 that extends its half-life is feasible and essential for boosting CAR-T cell antitumor activity in vivo.

In recent years, nanomaterials have played a significant role in inhibiting tumor growth by improving the immune state of the TME. Nanomaterials can enhance local and systemic antitumor immunity by targeting immune cells rather than directly acting on cancer cells.[14] Growing evidence suggests that the introduction of nanotechnology provides a new approach for optimizing CAR-T cell therapy by promoting CAR-T cell expansion and activation. Nanomaterials have been reported to significantly improve the preparation, delivery, and targeting of CAR-T cells, owing to their unique physical and chemical properties.[15] Therefore, a combination of nanopreparations with CAR-T cells to normalize the TME may significantly improve the efficacy of immunotherapy. Metal ion-based nanomaterials have been demonstrated to exert protective effects against disease progression, particularly in the context of antitumor therapy.[16] For example, manganese and certain nanoparticle-based nanomaterials can catalytically decompose endogenous H_2O_2 into O_2, thereby ameliorating hypoxic conditions.[17–19] Additionally, Mn^{2+} has been shown to exhibit a magnetic resonance tracer effect, enhancing T_1 magnetic resonance imaging (MRI) signals,[20] which can facilitate precise tumor localization and monitoring of the treatment effects.

A type of pH-dissociable calcium-based biominerals, $CaCO_3$ nanoparticles (NPs) have been explored for diverse biomedical applications because of their outstanding biodegradability.[21,22] $CaCO_3$ NPs are considered promising candidates for sustained neutralization of tumor acidity because of their high proton scavenging capacity. The biological roles of calcium ions (Ca^{2+}) as essential trace elements have been extensively investigated, including their involvement in the regulation of intracellular signaling, cellular homeostasis, and cellular immunity, which collectively determine the proliferation, metabolism, and death of various cells.[23,24] Furthermore, $CaCO_3$ NPs can remodel the immunosuppressive TME and energy metabolism of cancer cells, as well as enhance the antitumor immune response.[25] Moreover, the overaccumulation of Ca^{2+} released from $CaCO_3$ NPs can effectively induce the release of damage-associated molecular patterns from tumor cells via mitochondrial damage.[26–28] Thus, modifying the TME with nanotechnology may prove an effective strategy for combating tumors and augmenting the efficacy of immunotherapy.

In this study, we developed a pH-responsive biodegradable nanomaterial, $CaMnCO_3$ (CMC) NPs loaded with IL-21 (CMC-21), which exhibited positive regulatory effects against suppressive TME. We used flow cytometry, immunofluorescence, co-culture, western blotting, and tumor-bearing mouse models to illustrate the antitumor effects of CAR-T cells combined with CMC NPs. CMC-21 NPs were utilized as vitality backpacks to help CAR-T cells synergistically alleviate the immunosuppressive microenvironment and enhance HCC immunotherapy (**Scheme 1**). CMC NPs consume protons in the acidic TME to normalize its pH, alleviate intra-tumor hypoxia by catalyzing the decomposition of H_2O_2 to O_2, and awaken the innate immune system, which further decreases the expression of HIF-1α and promotes the tumor-associated macrophage (TAM) polarization from the M2 to M1 phenotype. The acid-responsive release of IL-21 exhibited a distinctive advantage, namely, the effective prolongation of the IL-21 half-life and safeguarding of its efficacy. Notably, IL-21 augmented the cytotoxic capability and central memory phenotype of CAR-T cells, improved their proliferative capacity, and reduced their exhaustion, resulting in superior in vitro and in vivo antitumor activity in HCC. CMC-21 exhibited a synergistic therapeutic effect greater than the sum of its parts, facilitating the activation of CAR-T cell-mediated antitumor immunity. Therefore, the combination of nanomaterials and CAR-T immunotherapy may offer novel therapeutic avenues for future clinical applications.

D. Li
Department of ICU
Shandong Provincial Hospital Affiliated to Shandong First Medical University
Jinan, Shandong 250021, P. R. China
Y. Sun
Urology Department
Shandong Provincial Hospital
Cheeloo College of Medicine
Shandong University
Jinan, Shandong 250021, P. R. China
H. Liu, J. Qi, S. Zhao
Department of Central Laboratory
Shandong Provincial Hospital Affiliated to Shandong First Medical University
Jinan, Shandong 250021, P. R. China
E-mail: songbosz@163.com
J. Duan
Institute for Advanced Interdisciplinary Research
University of Jinan
Jinan 250022, P. R. China
E-mail: iair_duanjz@ujn.edu.cn
Q. Zhu
Department of Infectious Disease
Shandong Provincial Hospital Affiliated to Shandong First Medical University
Jinan, Shandong 250021, P. R. China
E-mail: zhuqiang@sdu.edu.cn

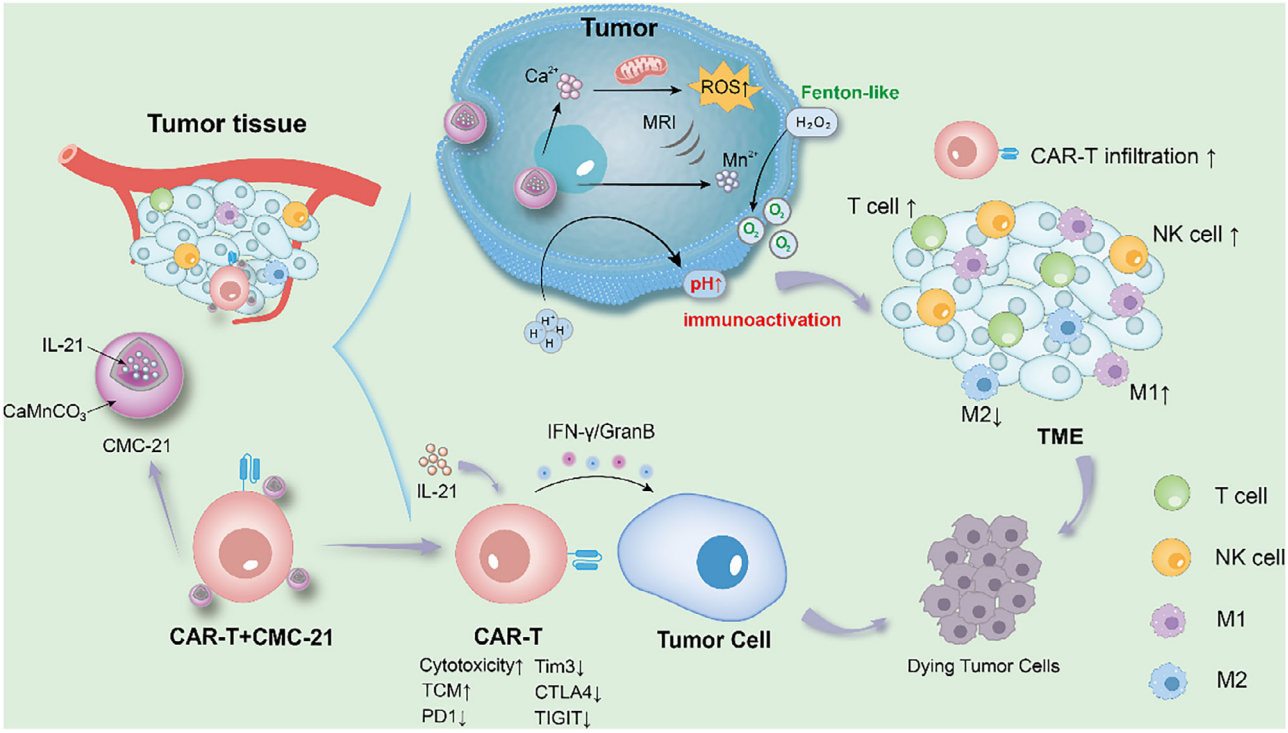

Scheme 1. Vitality backpacks of CMC-21 NPs boost CAR-T cell synergistic immunotherapy through TME promotion and sustained immunoactivation.

2. Results and Discussion

2.1. Synthesis and Characterization of CMC

Transmission electron microscopy (TEM) and high-resolution TEM (HRTEM) images of the synthesized CMC NPs are shown in **Figure** 1a,b respectively. TEM revealed that the CMC NPs had a highly porous structure, which endowed them with excellent absorption ability. The CMC NPs are rod-like and the pores with variable size distribute homogeneously on the surface of CMC NPs. The large amount of pore endows the CMC NPs with IL-21 absorption ability. The HRTEM image indicated that the synthesized CMC NPs possessed good crystallinity. The X-ray diffraction pattern of the CMC NPs in Figure 1c indicates their excellent crystallinity, which corresponds to that of the standard $CaCO_3$ material (PDF#29-0305). The elemental distributions of Ca and Mn in the CMC NPs were analyzed and shown in Figure 1d, which indicates the actual composition of the nanomaterials. The surface functional groups of the poly (acrylic acid) modified CMC nanomaterials were characterized using Fourier-transform infrared spectroscopy (Figure 1e). The strong peak located at 1394.3 cm^{-1} confirmed COO- absorbance on the surface of CMC NPs, which endowed the CAR-T cells with chemical conjugation ability. The Ca and Mn valence states in CMC X-ray photoelectron spectroscopy patterns (Figure 1f,g) indicate the coexistence of Ca^{2+} and Mn^{2+} in CMC, which corresponds to the elemental composition. In addition, the Mn 2P scan indicated that Mn^{2+} was partially oxidized to Mn^{4+}. The CMC is classified as a Lewis base, that possesses an acidic pH neutralization ability. As shown in Figure 1h, pH was effectively elevated by CMC. Variations in the acid-neutralizing properties of CMC were further characterized. In conditions mimicking, the TME (pH = 5.5), the zeta potential of CMC increased from −24 to −8.29 mV (Figure 1i). Both the size distribution (Figure 1j) and Uv–vis absorption (Figure 1k) decreased, indicating decomposition of the CMC nanostructure. In addition, as shown in Figure S1 (Supporting Information), the TEM images of CMC NPs after treatment with pH = 5.5 PBS showed the CMC decomposition residues. These results confirmed the acid-responsive properties of CMC. Owing to the presence of Mn^{2+} in its structure, CMC effectively generated O_2 via H_2O_2 catalytic reaction (Figure S2, Supporting Information), which further alleviated TME hypoxia. The abundant carboxyl groups on the surface of CMC NPs allowed their chemical modification. As shown in Figure S3 (Supporting Information), there were many CMC NPs on the surface of CAR-T cells, forming vitality backpacks.

2.2. CMC NPs Induced Tumor Cell Death by Disturbing Mitochondrial Homeostasis

It is reported that Ca & Mn nanostimulators have antitumor ability in vivo.[25] To investigate the in vitro activity of CMC NPs, we first evaluated the toxicity of CMC NPs to tumor cells. The mouse hepatoma cell line hepa1-6, embryonic fibroblast cell line NIH3T3, and breast carcinoma cell line 4T1 were treated with different doses of CMC NPs. The results showed a dose-dependent increase in apoptosis (**Figure** 2a–c). The CCK8 assay showed a decline in tumor cell viability after co-incubation with high concentrations of CMC NPs. (Figure 2a,b). Flow cytometry illustrated that the number of apoptotic cells significantly increased upon stimulation with high concentrations (5 μg mL^{-1}

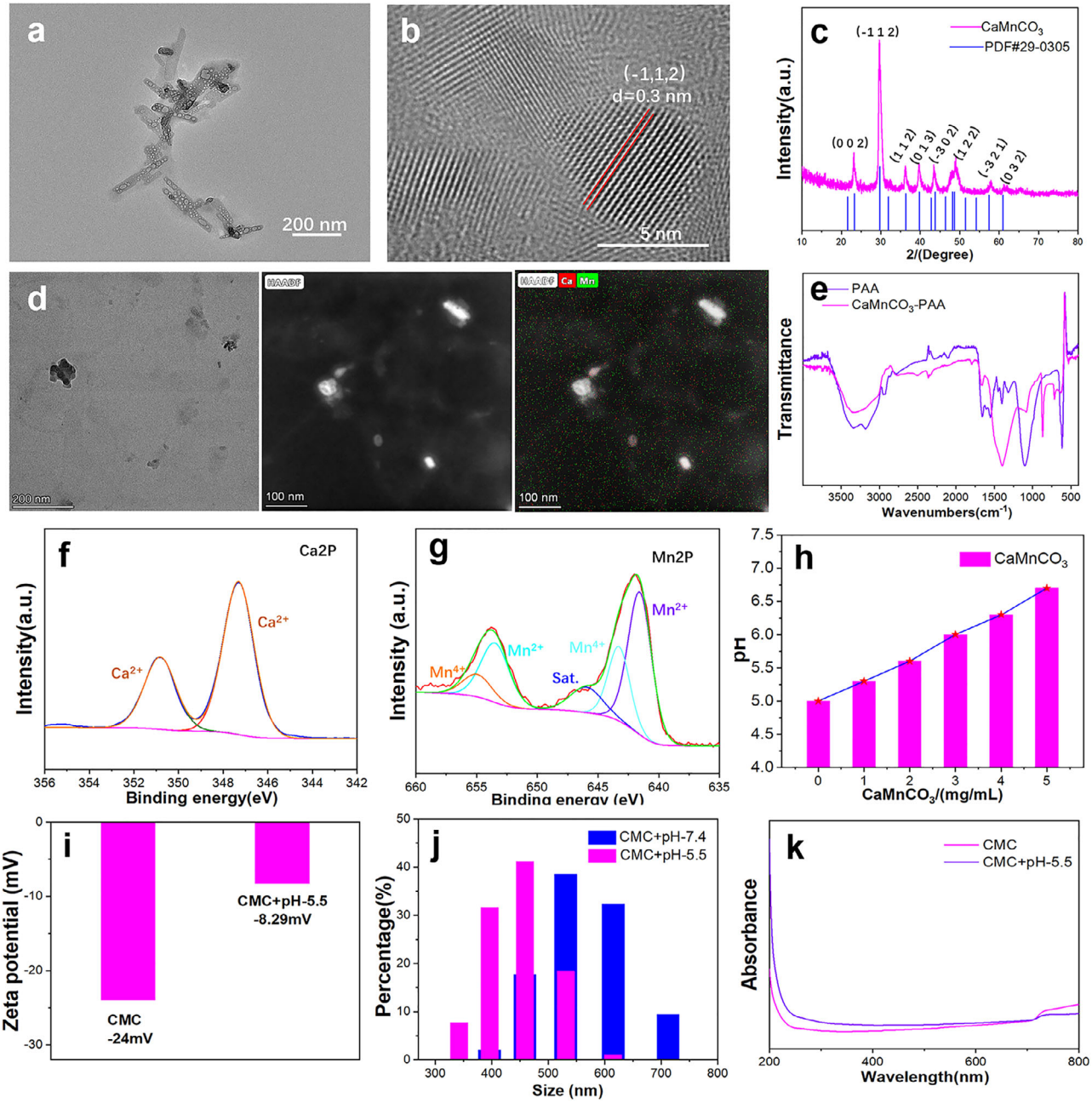

Figure 1. Characterization of CMC NPs. a) TEM and b) HRTEM image of synthesized CMC NPs. c) XRD pattern of CMC NPs. d) Element distribution in CMC NPs. e) FTIR pattern of CMC NPs. f) Ca2P and g) Mn2P XPS pattern of CMC NPs. h) The acidity pH neutralization by CMC NPs. i) Zeta potential value, j) size distribution, and k) UV–vis absorbance of CMC NPs (pH = 7.4) and CMC NPs treated with acidity condition (pH = 5.5).

or more) of CMC NPs (Figure 2c). Western blotting further confirmed that high concentrations of CMC NPs promoted apoptosis (Figure 2d,e). Taken together, these results indicated that elevated CMC NP levels induce apoptosis in cancer cells.

Ca^{2+} causes mitochondrial Ca^{2+} overload, which amplifies the oxidative stress.[29] To further verify whether CMC NPs affect mitochondria, the mitochondrial function of tumor cells was assayed. The results showed that CMC NPs significantly increased reactive oxygen species (ROS) levels in tumor tissue sections, as well as in hepa1-6 and 4T1 cells while reducing mitochondrial oxygen consumption (Figure 2f–h). Mitochondrial transcription factor A (TFAM) is essential for the maintenance, expression, and transmission of mitochondrial DNA.[30,31] Abnormal Mitochondrial import receptor subunit TOM20 homolog (TOM20) expression is associated with deficient mitochondrial respiration and loss of mitochondrial membrane potential.[32] We found that TFAM and TOM20 were expressed lowly in hepa1-6 cells incubated with CMC NPs (Figure 2i,j). Meanwhile, CMC NPs decreased the mitochondrial membrane potential ($\Delta\Psi m$) of hepa1-6 cells (Figure 2k). To investigate whether CMC NPs affect tumor

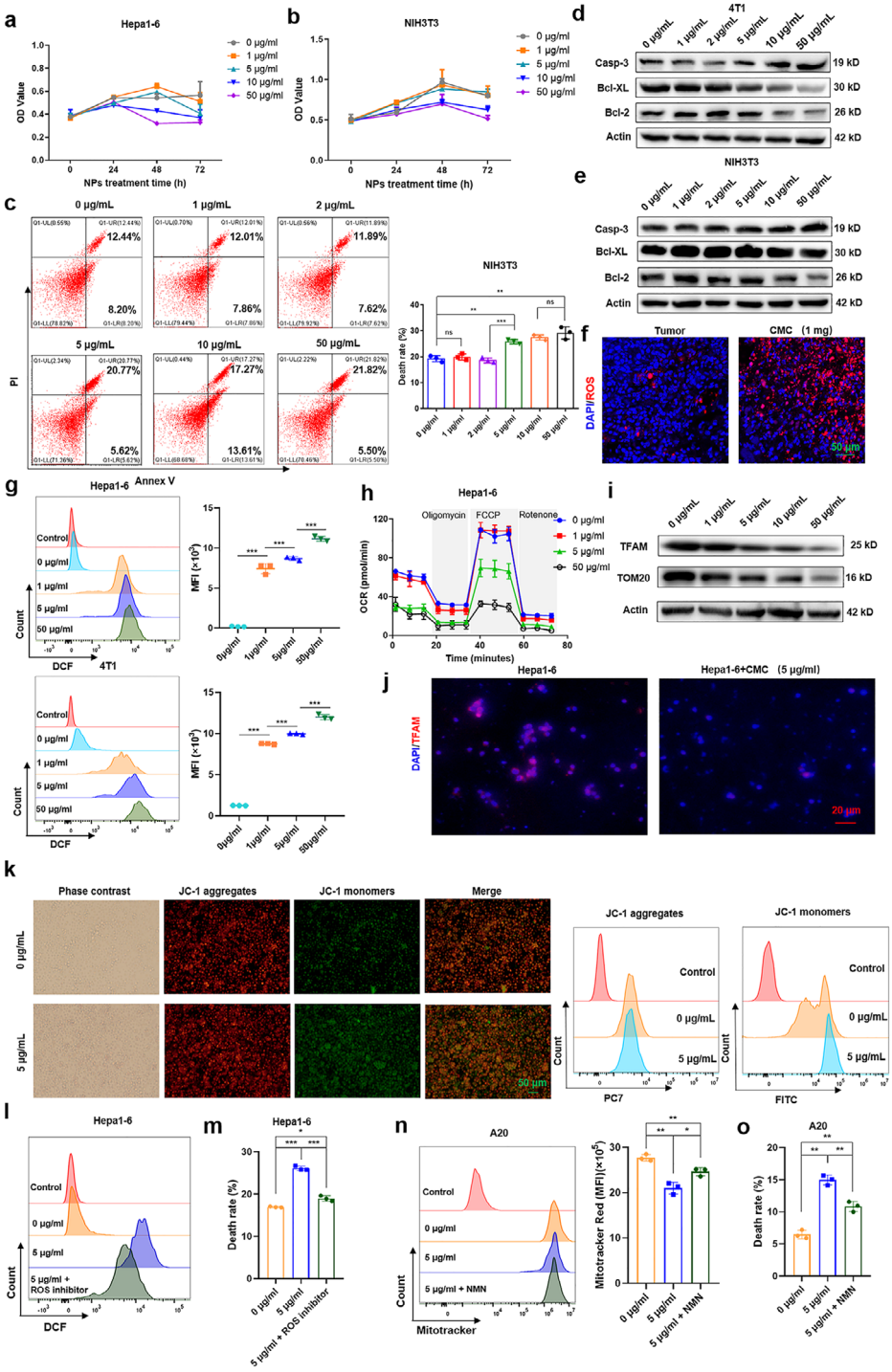

Figure 2. CMC NPs induced tumor cell death by disturbing mitochondrial homeostasis. Proliferation analysis of Hepa1-6 a) and NIH3T3 b) cells treated with different levels of CMC NPs using a CCK-8 assay. c) NIH3T3 cells were treated with CMC NPs (0, 1, 2, 5, 10, and 50 μg mL^{-1}) for 24h, and apoptosis was assayed using the apoptosis detection kit. The caspase-3, Bcl-XL, and Bcl-2 of 4T1 d) and NIH3T3 e) were analyzed. f) The ROS of HCC tumor tissue sections was assayed. The Balb/c mice were subcutaneously injected with hepa1-6 cells into the right flank, and seven days later, mice were injected intravenously with 1 mg CMC NPs in 100 μL PBS or PBS. Three days later, mice were euthanized and tumors were isolated. g) CMC NPs improved the levels of ROS in hepa1-6 and 4T1 cells. h) OCR of hepa1-6 cells at baseline and in response to oligomycin, FCCP, and rotenone. i) The TFAM and TOM20 of hepa1-6 cells treated with CMC NPs were analyzed by western blotting. j) The TFAM of hepa1-6 cells treated with CMC NPs was detected by immunofluorescent staining. k) JC-1 staining to detect mitochondrial member potential using a fluorescence microscope and flow cytometry. The ROS l) and death rate m) of hepa1-6 cells incubated with or without ROS-IN-2 (1 μg mL^{-1}) were detected. The MitoTracker n) and death rate o) of A20 cells with or without NMN were detected. The data presented are the mean ± SD of three separate experiments. ns means no significant difference, $^{*}p < 0.05$, $^{**}p < 0.01$, $^{***}p < 0.001$ compared with indicated group.

cell apoptosis by regulating mitochondrial function, an ROS scavenging reagent (ROS-IN-2) and nicotinamide mononucleotide (NMN) were used (Figure 2l–o). The death rate of hepa1-6 cells was reduced by ROS-IN-2 treatment (Figure 2m). NMN can enhance cellular oxidative phosphorylation and reduce the production of cellular ROS.[33] In this study, ROS inhibition reduced the apoptotic rate of A20 cells (Figure 2o; Figure S4a, Supporting Information). MitoTracker Red staining and flow cytometry demonstrated that NMN treatment decreased mitochondrial dysfunction and apoptosis in A20 cells (Figure 2n,o; Figure S4b, Supporting Information). These findings suggested that CMC NPs induced tumor cell apoptosis by regulating mitochondrial homeostasis.

2.3. Appropriate Concentration of CMC NPs Does Not Affect CAR-T Cell Cytotoxicity

CMC NPs are toxic to tumor cells, and we examined whether they affect the viability and function of CAR-T cells. CAR-T cells targeting GPC3 (glypican 3) and FAP (fibroblast activation protein) were generated (Figures S4c,d and S5a,c, Supporting Information). FAP is a membrane protease highly expressed in cancer-associated fibroblasts and regulates the TME by remodeling the extracellular matrix.[34] As a cell-surface protein, GPC3 highly expressed a large proportion of HCC cells but hardly expressed in normal adult tissues.[35,36] FAP and GPC3 are significant diagnostic molecular markers and immunotherapeutic targets in HCC.[37,38] In vitro experiments showed that GPC3 CAR-T cells obviously inhibited the growth of hepa1-6 cells (Figure S4e, Supporting Information). To evaluate the specificity of the antitumor activity of FAP CAR-T cells, the FAP overexpressing 4T1 and hepa1-6 cell lines were established (4T1-FAP and hepa1-6-FAP) (Figure S5b, Supporting Information). When FAP CAR-T cells were co-cultured with 4T1-FAP cells at an effector:target (E:T) ratio of 1:1, they showed obvious cytotoxicity toward 4T1-FAP cells (Figure S5d, Supporting Information). Simultaneously, the levels of IFN-γ and granzyme B significantly increased in supernatants released by FAP CAR-T cells. Degranulation is a requisite process in perforin-granzyme-mediated apoptosis (**Figure 3f**; Figure S5e, Supporting Information). We found that CD107a was extraordinarily expressed on the surface of FAP CAR-T cells in response to 4T1-FAP cells (Figure S5g, Supporting Information). Overall, these data confirmed that the engineered GPC3 and FAP CAR-T cells retained superior tumor lysis abilities in vitro.

The CMC NPs showed toxicity to tumor cells by regulating mitochondrial homeostasis, however, whether CMC NPs are toxic to CAR-T cells is unknown. To assess the effect of CMC NPs on CAR-T cells, GPC3 CAR-T cells were co-cultured with different CMC NPs concentrations. The findings revealed that CAR-T cell apoptosis was unaffected by CMC NPs at concentrations of 0, 1, 2, and 5 μg mL^{-1}. However, when exposed to 10 μg mL^{-1} CMC, CAR-T cell apoptosis markedly increased (Figure 3a,b). In addition, the lower concentrations (5 μg mL^{-1} or less) of CMC NPs did not influence the cytotoxicity of GPC3 CAR-T cells (Figure 3c), which was consistent with the release of granzyme B (Figure 3d), indicating that CAR T-cell cytotoxicity was unaffected by CMC NP concentrations ≤ 5 μg mL^{-1}. To further identify different phenotypes and mRNA expression, we performed genome-wide transcriptional profiling analysis of GPC3 CAR-T cells (unstimulated by antigens or tumor cells) with or without CMC NPs (5 μg mL^{-1}). Principal component analysis (PCA) and violin plots indicated that the differences within individual groups of samples were quite small (Figure 3e,f). Compared with levels in the CAR-T group, 57 genes were upregulated and 23 downregulated gene in CAR-T cells stimulated with CMC NPs (Figure 3g; Tables S1 and S2, Supporting Information). The differentially expressed genes from the comparison between the GPC3 CAR T-cells group and CAR T cells stimulated with CMC NPs were significantly involved in five downregulated and two upregulated signaling pathways (Figure 3h,i). After careful analysis, the signaling pathways showed no significant differences, demonstrating that 5 μg mL^{-1} CMC NPs had no obvious effects on transcription in CAR-T cells.

In summary, the appropriate concentrations of CMC NPs did not affect the activity and killing function of CAR-T cells.

2.4. CMC-21 NPs Combined with CAR-T Cells Effectively Inhibits HCC In Vivo

Based on the satisfactory therapeutic effects observed in vitro, we further confirmed the ability of CAR-T cells combined with CMC-21 to specifically inhibit tumor growth in vivo. First, the loading efficiency and release efficiency of CMC-21 were evaluated (Figure S6, Supporting Information). Owing to the slightly acidic character of the TME, the loaded IL-21 was gradually released from the nanoplatform following the degradation of the CMC-21 NPs under acidic conditions. Irradiated mice were subcutaneously injected with hepa1-6-FAP and treated with CAR-T cells or CMC-21 combined with CAR-T cells (**Figure 4a**). By monitoring tumor size, we found that the combination of CMC-21 and CAR-T cells was most effective in inhibiting tumor growth (Figure 4b,c), and there was no significant change in the body weight of mice in each group (Figure 4d). As described in Figure 4e, the tumors in the FAP CAR-T combined with the CMC-21 group were smaller than those in the other groups on day 10. The median survival times of mice in the PBS, CMC-21, CAR-T, and CAR-T+CMC-21 groups were 12.8, 15.4, 25.4, and 32.4 days, respectively (Figure 4f), indicating that FAP CAR-T cells assisted by CMC-21 NPs obviously extend the overall survival time. Tumor tissues treated with CAR-T cells and CMC-21 NPs expressed enhanced caspase-3 and lower Ki67, Bcl-XL, and Bcl-2 (Figure 4g), illustrating that CAR-T cells combined with CMC-NPs prompted tumor cells to die and deprived them of their proliferative capacity. For further comparative investigation, cell necrosis and apoptosis in tumor sections were examined using H&E, Ki67, and TUNEL staining (Figure 4h). In addition, ROS levels in tumor tissues were detected and were elevated in the CAR-T cell + CMC-21 group (Figure 4i). Taken together, these results demonstrated that the antitumor efficiency of systemically administered CAR T cells was significantly enhanced when combined with CMC-21 NPs.

To further evaluate the broad effect of the combination of CAR-T cells and CMC-21NPs, a high-burden xenograft model was established by subcutaneous injection of hepa1-6 cells. Five days after tumor-bearing, the mice received one lower dose of GPC3 CAR-T cells combined with CMC-21 NPs. Seven days

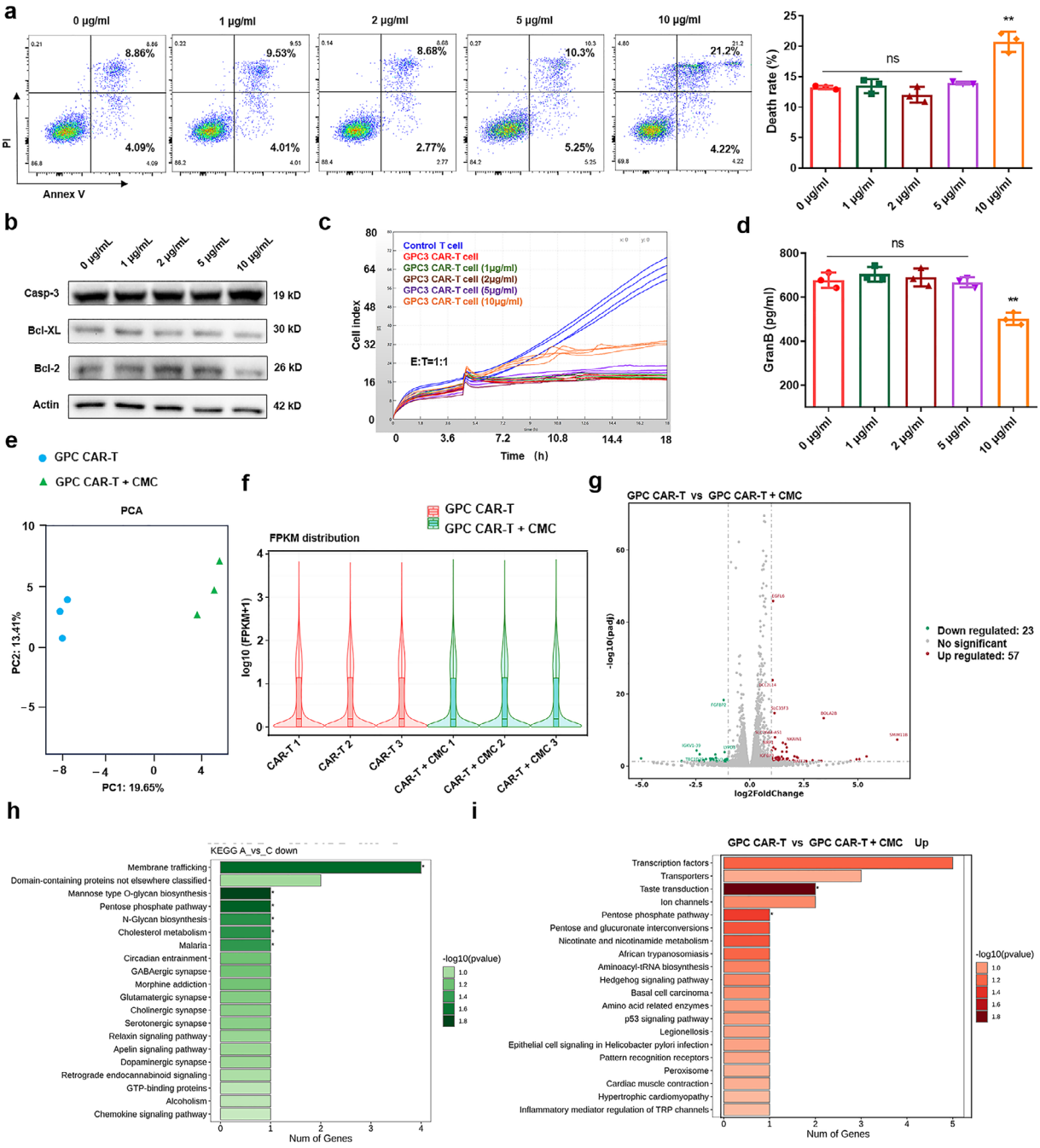

Figure 3. The effect of CMC NPs on cytotoxicity and gene expression of CAR-T cells. (a) GPC3 CAR-T cells were treated with CMC NPs (0, 1, 2, 5, 10, and 50 μg mL^{-1}) for 12 h, and apoptosis was assayed using the apoptosis detection kit. b) The caspase-3, Bcl-XL, and Bcl-2 of GPC3 CAR-T cells treated with CMC NPs were analyzed. c) Cytotoxicity of GPC3 CAR-T cells incubated with CMC NPs to hepa1-6 cell at E:T ratio of 1:1 was assayed using real-time monitor. d) ELISA was performed to measure granzyme B in the supernatants from GPC3 CAR-T cells cocultured with hepa1-6 cells incubated with CMC NPs for 18 h. e) The PCA analysis. f) The violin plot. g) The volcano plot. The down signaling pathways h) and up signaling pathways i) of KEGG analysis. The data presented are the mean ± SD of three separate experiments. ns means no significant difference, $^{*}p < 0.05$, $^{**}p < 0.01$, $^{***}p < 0.001$ compared with indicated group.

after infusion, the mice were humanely euthanized, and the tumors were isolated (**Figure 5**a). As shown in Figure 5b,c,e, CAR-T cells combined with CMC-21 NPs significantly controlled tumor growth and extended overall survival. In addition, the tumors of mice treated with GPC3 CAR-T cell + CMC-21 were obviously smaller than those in the other groups in a parallel experiment (Figure 5d). Meanwhile, H&E staining of the hearts, livers, spleens, lungs, and kidneys showed no obvious toxicity to the major organs (Figure 5f). In summary, the combination of CMC-21 NPs and CAR-T cells effectively suppressed

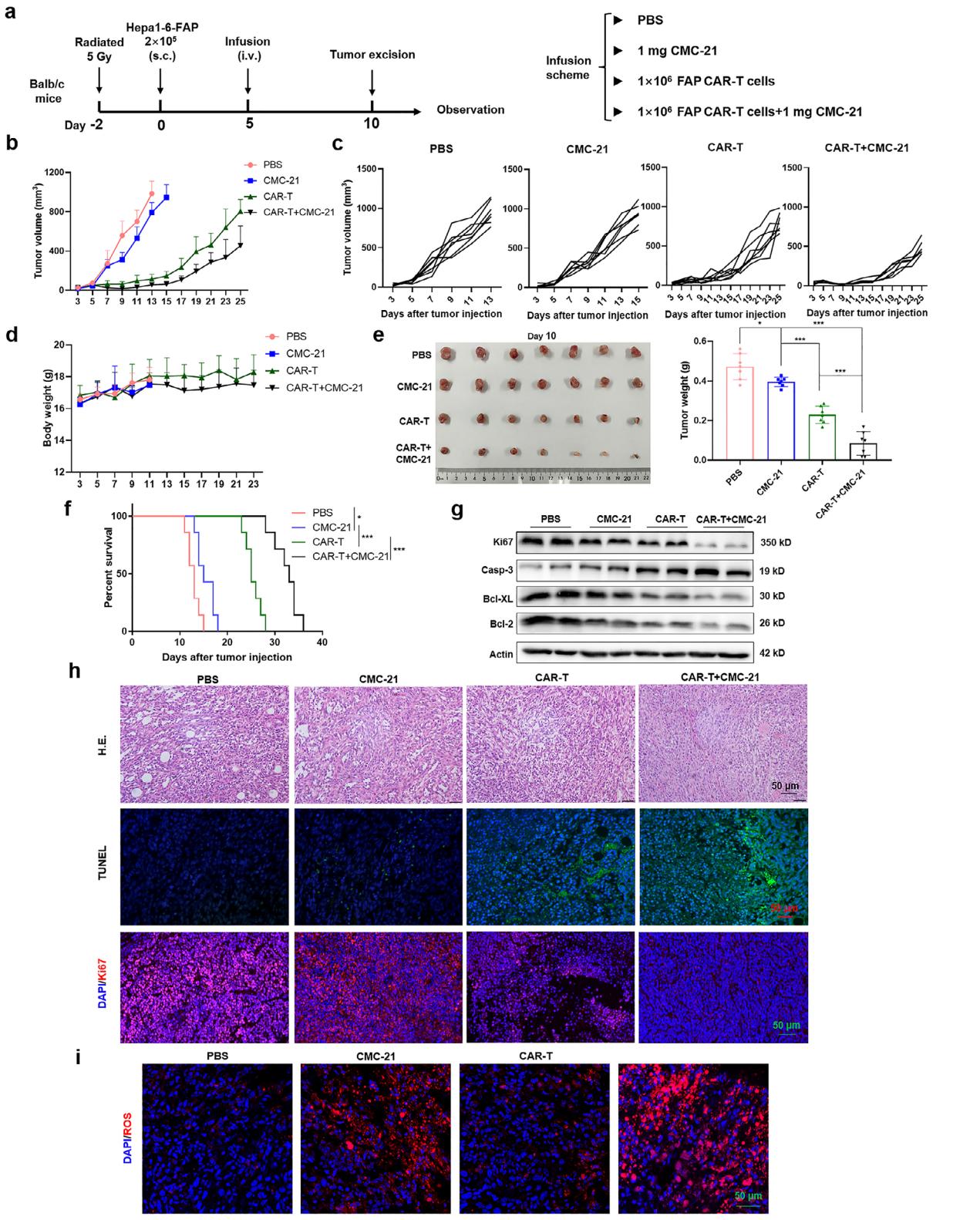

Figure 4. CMC-21 NPs combined with CAR-T effectively inhibit HCC in vivo. a) Experimental design. b,c) Tumor size was measured once every 2 days. d) The body weights of the mice were measured. e) Images of tumor-bearing mice and tumor weight ($n = 7$). f) Survival curve of tumor-bearing mice, and statistical analysis was performed using the log-rank (Mantel–Cox) test. g) The ki67, caspase-3, Bcl-XL, and Bcl-2 of tumor tissues were analyzed by western blotting. h) Tissue pathology of the tumors. i) The ROS of tumor tissue sections was analyzed. Magnification: × 400. (Scale bar, 50 μm). The data presented are the mean ± SD of three separate experiments. ns means no significant difference, $^{*}p < 0.05$, $^{**}p < 0.01$, $^{***}p < 0.001$ compared with indicated group.

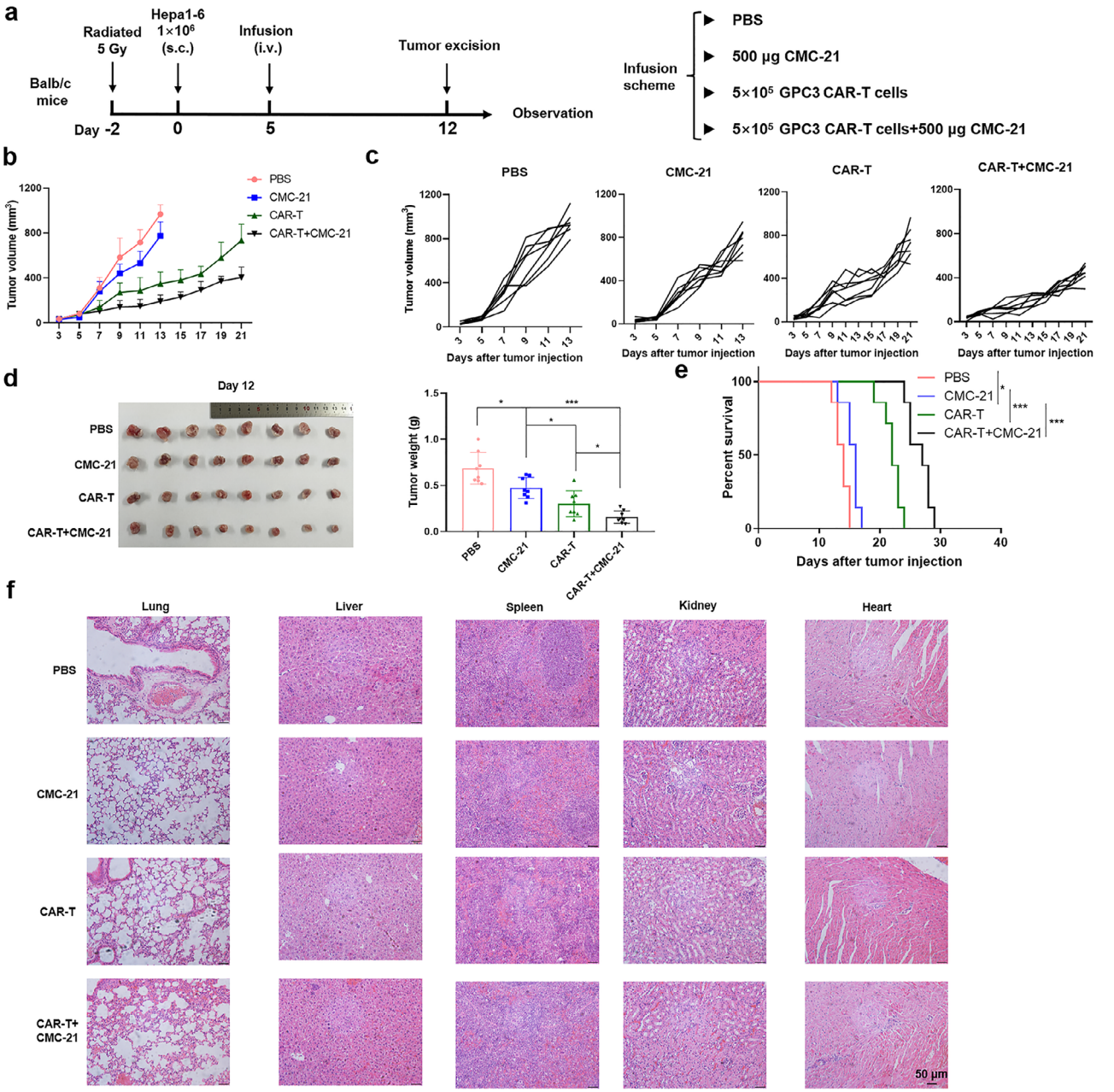

Figure 5. CMC-21 NPs combined with CAR-T effectively inhibited high-burden HCC. a) Experimental design. b,c) Tumor size was measured once every 2 days. d) Images of tumor-bearing mice and tumor weight ($n = 8$). e) Survival curve of tumor-bearing mice, and statistical analysis was performed using the log-rank (Mantel–Cox) test. f) Tissue pathology of the main organs and tissues. Lung, liver, spleen, kidney, and heart were evaluated by H&E staining. Magnification: ×400. (Scale bar, 50 μm). ns means no significant difference, $^{*}p < 0.05$, $^{**}p < 0.01$, $^{***}p < 0.001$ compared with indicated group.

hepatocellular carcinoma, exhibiting synergistic effects in combating tumors.

2.5. CMC NPs Remodel TME by Elevating pH and Producing O_2

The TME is characterized by hypoxia and low pH. Given that CMC-21 NPs synergize with CAR-T cells to produce a promising antitumor effect, we investigated the properties of CMC NPs at the cellular level to further explore the mechanism by which they improve the TME. For TME, Mn ion-based nanomaterials act as nanozymes to relieve hypoxia by decomposing intracellular H_2O_2 to remodel the TME.[39,40] Taking advantage of the catalytic reaction of CMC NPs with H_2O_2 in vitro (Figure S2, Supporting Information), we investigated whether CMC NPs could effectively improve the hypoxic TME. HIF-1α acts as a key transcription factor for evaluating the state of cellular hypoxia. HIF-1α expression in hepa1-6 and 4T1 cells cultured in a hypoxic environment was investigated, and the results showed that CMC alleviated the hypoxia (**Figure** 6a–c). Lower HIF-1α expression

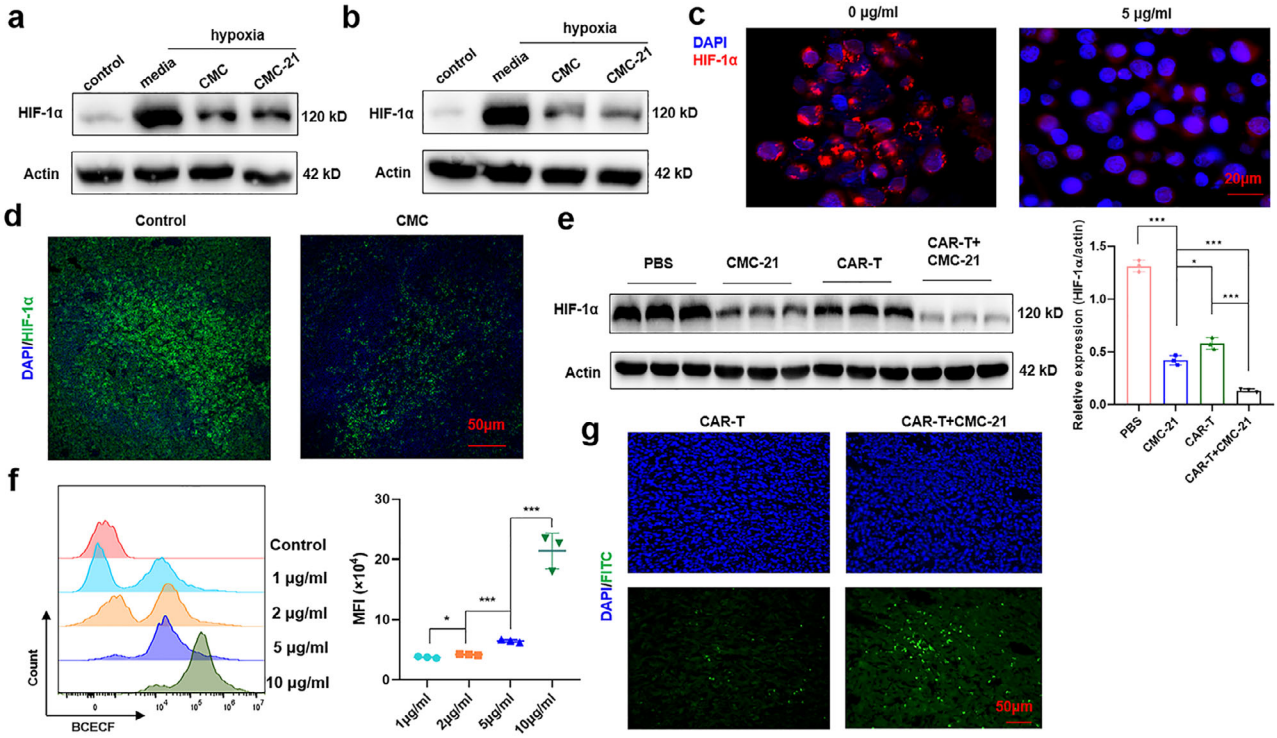

Figure 6. CMC NPs remodel TME by elevating pH and producing O2. The HIF-1α expression of hepa1-6 a) and 4T1 b) was detected in hypoxia conditions. c) The HIF-1α expression of A20 cells was analyzed using immunofluorescence. The HIF-1α expression of tumor tissues was analyzed using immunofluorescence d) and western blotting e). f) The pH value of hepa1-6 cells cultured in DMEM media added with 0.2% H_2O_2 was analyzed using flow cytometry. g) The pH value detection of tumor tissues. Magnification: ×400. (Scale bar, 50 μm). Data presented are the mean±SD of three separate experiments. ns means no significant difference, $^{*}p < 0.05$, $^{**}p < 0.01$, $^{***}p < 0.001$ compared with indicated group.

was also detected in tumor tissues treated with CAR-T cells plus CMC-21 NPs (Figure 6d,e), indicating that CMC effectively relieved the hypoxic microenvironment of the tumor tissues.

$CaCO_3$ is a biocompatible nanomaterial that reduces the acidity in the TME by reacting with protons and increasing pH, contributing to ROS generation, and subsequently amplifying intracellular oxidative stress.[41] CMC NP degradation occurred rapidly in a pH = 5.5 solution (Figure S1, Supporting Information). As shown in Figure S2 (Supporting Information), the decomposition of H_2O_2 by CMC NPs was measured by adding CMC NPs to an H_2O_2-containing PBS solution. The appearance of bubbles indicated the decomposition of H_2O_2 and the generation of oxygen. In this study, CMC NPs increased the pH of hepa1-6 cells cultured in DMEM media supplemented with 0.2% H_2O_2 (Figure 6f), because the CMC NPs effectively consume excess cellular protons. The in vivo experiments showed that CMC-21 elevated the pH of the TME upon treatment with CAR-T cells (Figure 6g), suggesting an excellent acidity-attenuating effect of the CMC NPs in vivo.

2.6. CAR-T Cells Combined with CMC-21 NPs Improved the Immunosuppressive TME

The alleviation of hypoxia in the TME can be realized by increasing O_2 production derived from the catalytic reaction between CMC NPs and H_2O_2 in tumor tissues. To investigate the effect of CMC NPs on the immune status of the TME, a hepa1-6-FAP tumor-bearing mouse model was established (**Figure 7a**). After FAP CAR-T cell injection, the immune cells in the tumor tissues were analyzed using flow cytometry (Figure S7, Supporting Information). The results showed that compared with the CMC-NPs and FAP CAR-T cell groups, treatment with CAR-T cells combined with CMC-21 NPs significantly enhanced the infiltration of extrinsic CAR-T cells as well as intrinsic immune cells (i.e., murine $CD4^+$ T cells, $CD8^+$ T cells, and NK cells) (Figure 7b–d). Consistently, IFN-γ and granzyme B levels in supernatants from tumor tissue homogenates were significantly upregulated in the FAP CAR-T cell + CMC-21 group compared with levels in the control groups (Figure 7e). These results indicated that CAR-T cell + CMC-21 can remodel the tumor immune microenvironment by improving hypoxia and increasing pH, thus further enhancing immune cell infiltration.

Among the immunosuppressive cells in the TME, the M2-like TAMs are usually contributing to tumor development.[42,43] Immunosuppressive cells promote tumor progression by inhibiting antitumor immune response. In addition, It is reported that M2 macrophages can be polarized to M1 macrophages by elevated ROS and O_2 levels in the TME.[9] Therefore, reprogramming TAMs from the M2 to M1 phenotype is crucial to promoting effective tumor therapy by remodeling the TME. Mn oxide NPs induce a certain level of TAM polarization. Elevated levels of M1-like macrophages were observed in the Fap CAR-T cell + CMC-21 group. FAP CAR-T cell + CMC-21 treatment also

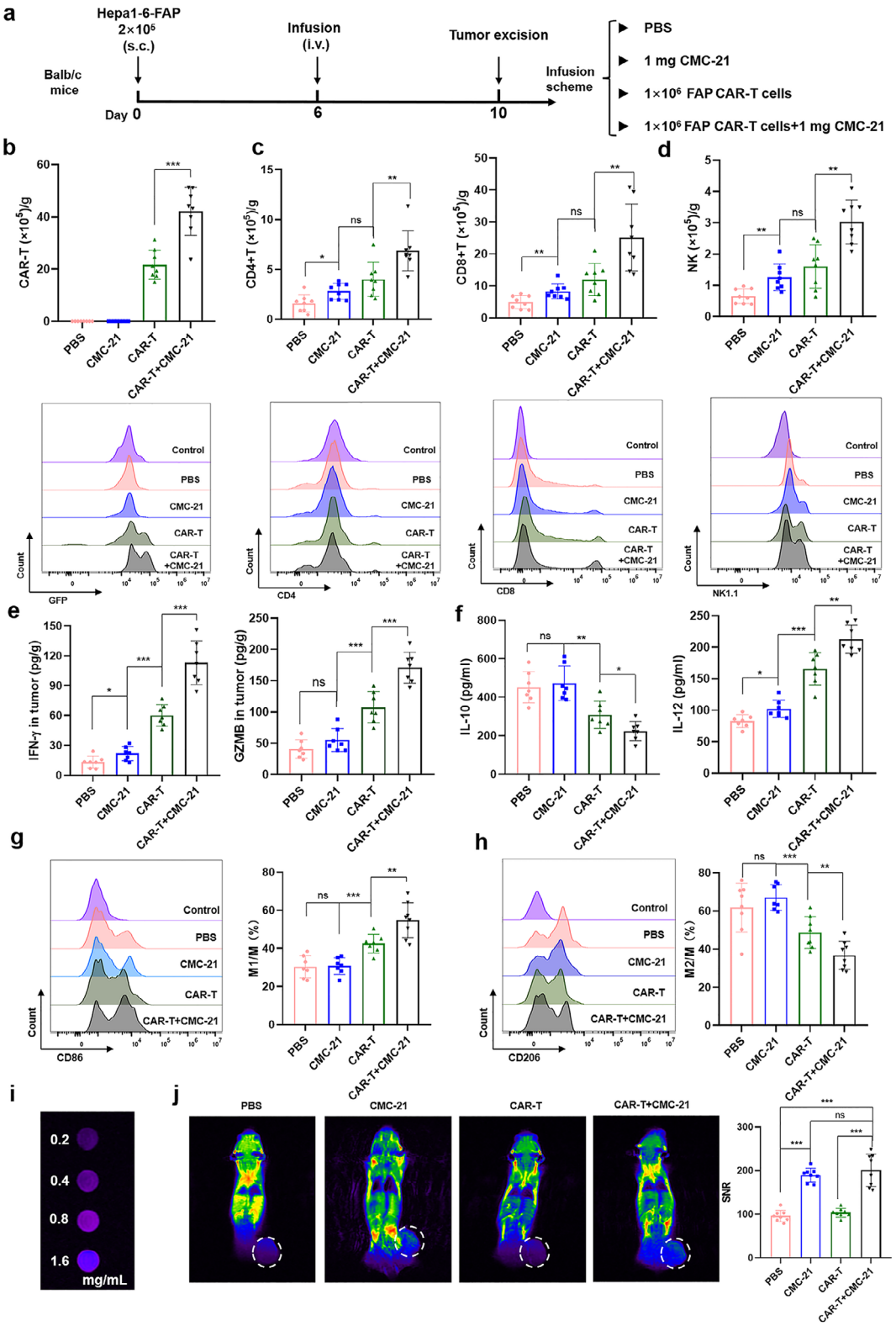

Figure 7. CAR-T cells combined with CMC-21 NPs improved immunosuppressive TME. a) Experimental design. Injected CAR-T cells b), $CD4^+$ CAR-T cells, $CD8^+$ T cells c), and intrinsic NK cells d) in tumor tissues were assayed. The levels of IFN-γ, granzyme B e), IL-10, and IL-12 f) in the supernatants of tumor lysates were analyzed by ELISA. The M1-like macrophages ($CD45^+$ $CD11b^+$ $F4/80^+$ $CD86^+$) g) and M2-like macrophages ($CD45^+$ $CD11b^+$ $F4/80^+$ $CD206^+$) h) in tumor tissues were analyzed. i) The T1 MRI images of different densities of CMC NPs. j) The T1 mode MRI images of tumor-bearing mice in the tumor. ns means no significant difference, $^*p < 0.05$, $^{**}p < 0.01$, $^{***}p < 0.001$ compared with indicated group.

efficiently polarized TAMs from the immune-suppressive M2-like phenotype ($CD45^+$ $CD11b^+$ $F4/80^+$ $CD206^+$) to the immune-supporting M1-like phenotype ($CD45^+$ $CD11b^+$ $F4/80^+$ $CD86^+$) (Figure 7g,h). IL-12, a cytokine predominantly secreted by M1-like TAMs in the supernatants of tumor lysates, was also significantly upregulated in the FAP CAR-T cell + CMC-21 group, whereas IL-10, a cytokine mainly secreted by M2-type TAMs, was significantly downregulated,[19] indicating significant M1 polarization of TAMs within tumor tissues after treatment with CAR-T cells combined with CMC-21 NPs (Figure 7f). Next, MRI scanning was performed in a mouse model of hepa1-6-FAP to evaluate the CMC NP trace in vivo, and the T1 MRI ability of the CMC NPs was determined (Figure 7i). The results revealed that the CMC NPs displayed excellent T1 signals and could be used as T1 contrast agents. The MRI signals at the tumor sites in the mouse model after intravenous injection of CMC NPs and CAR-T cells individually and combined for 6 h are shown in Figure 7j. The signal intensities at the tumor sites were analyzed, and the results revealed that CMC NPs could enhance tumor diagnosis.

Taken together, these results indicated that CMC-21 NPs may be mainly recruited to the tumor tissues to remodel the TME by reducing hypoxia and increasing pH, further increasing CAR-T cell and other immunocyte infiltration and reprogramming TAMs, which synergistically and collaboratively enhance the antitumor effects of CAR-T cells.

2.7. CMC-21 NPs Improved CAR-T Cell Phenotype

The present study reported that IL-21 could improve CAR-T cell infiltration and enhance immune response via an immunofeedback pathway to robustly enhance antitumor immunotherapy in solid tumors.[44–46] We speculated that IL-21 was slowly and gradually released from the CMC-21 nanoplatform, with pH-responsive release characteristics in the TME. To analyze the effect of CMC-21 NPs on CAR-T cells, CMC NPs were loaded with IL-21 at a mass ratio ≈100:1. T cell exhaustion, which is commonly related to CAR-T cell persistence, is a state in which T cells gradually lose their effector function and self-renewal capacity because of prolonged exposure to tumor antigens.[47–49] We found that CMC-21 NPs down-regulated the expression of several immune effects of GPC3 CAR-T cells (e.g., PD-1, CTLA4, TIM3, and TIGIT) (**Figure** 8a–d), demonstrating the favorable effects of CMC-21 NPs in mitigating exhaustion in GPC3 CAR-T cells, with an effect similar to but greater than that of IL-21 alone.

Generally, a less-differentiated phenotype promotes T cell antitumor activity. T cells can be divided into four phenotypes according to CD62L and CD45RO expression.[50,51] To evaluate the potential advantages of T cells undergoing prolonged stimulation by tumor cells, the phenotypes were assayed using flow cytometry. IL-21- and CMC-21- activated GPC3 CAR-T cells were enriched in the less-differentiated TCM (center memory T cell) compartment with a high proportion of $CD45RO^+CD62L^+$ cells (Figure 8e; Figure S8, Supporting Information). Flow cytometry analysis showed the up-regulation of the key memory stem-like marker CCR7 in CAR-T cells co-cultured with CMC-21 NPs (Figure 8f). Meanwhile, higher levels of the low-differentiation associated costimulatory molecules CD27 and CD28[46] were expressed in GPC3 CAR-T cells treated with CMC NPs (Figure 8g,h), demonstrating that CMC-21 NPs and IL-21 were capable of promoting CAR-T cell differentiation toward a memory phenotype. In addition, the expression of the activation marker CD69 was enhanced in CAR-T cells stimulated with IL-21 and CMC-21 NPs (Figure 8i). Consistently, GPC3 CAR-T cells co-cultured with CMC-21 NPs maintained a more proliferative phenotype than did CAR-T cells alone (Figure 8j–l). Transwell assays were performed to confirm the ability of CMC-21 NPs to migrate into HCC cells. As expected, the migration of GPC3 CAR-T cells treated with CMC-21 NPs from the upper to the lower chamber inoculated with hepa1-6 cells obviously increased (green cells) (Figure 8m). These results demonstrated that CMC-21 NPs function just as IL-21 dose to improve CAR-T cell superior phenotype in vivo.

Taken together, IL-21 and CMC-21, endowed CAR-T cells with a more proliferative, less-exhausted, and less-differentiated phenotype than that in the control group, and the cells and nanoparticles joined together to maintain high cytotoxicity against their targets.

2.8. The Enhanced Antitumor Activity that IL-21 Provides to CAR T Cells Depends on its Gradual Release from CMC NPs

For some currently constructed drugs or cytokine-loaded nanomaterials, drug or cytokine release from the nanomaterials usually enhances antitumor activity. In this study, we designed a pH-responsive, sustained-release CMC for IL-21 delivery. The superior phenotype of CAR-T cells was a direct result of stimulation with CMC-21 NPs and was intrinsically dependent on IL-21 release. The results showed that IL-21 enhanced the cytotoxicity of FAP CAR-T cells in vitro (**Figure** 9a). The killing curves of GPC3 CAR-T cells stimulated with IL-21 and CMC-21 NPs were similar, and both were superior to those of unstimulated FAP CAR-T cells (Figure 9b), which was consistent with IFN-γ and granzyme B released trends (Figure 9c,d). Additionally, the same result was observed in vivo, where the sustained release of IL-21 from the CMC nanoplatform enhanced the antitumor function of CAR-T cells. The mice were injected with GPC3 CAR-T cell +1000 μg CMC + 10 μg IL-21 or GPC3 CAR-T cell + 1000 μg CMC-21 (loading ≈10 μg IL-21) (Figure 9e). As shown in Figure 9f,g, GPC3 CAR-T cells combined with CMC-21 significantly controlled tumor growth and extended overall survival compared to values achieved by CAR-T cells combined with IL-21. The sizes of tumors isolated on day 8 in mice treated with CAR-T cells combined with CMC-21 were smaller than those of the controls in parallel experiments (Figure 9h). Meanwhile, treatment with GPC3 CAR-T cells + CMC-21 NPs significantly enhanced intrinsic T cell infiltration compared with control groups (Figure 9i,j). The number of immune-supportive M1-like cells was elevated in the GPC3 CAR-T cells + CMC-21 NPs treatment group, indicating that antitumor immunity was effectively activated in CAR-T cells when they were combined with CMC-21 NPs.

We further tested the synergistic therapeutic effects of CAR-T cells and CMC-21 NPs in a spontaneous Balb/c mouse model of HCC. Figure 9k shows the establishment of an orthotopic liver tumor-bearing mouse model by using c-Myc overexpression and its treatment procedures. During treatment, the corresponding development of hepatic tumors in the various groups was evaluated using the IVIS Spectrum system. After 15 days of treat-

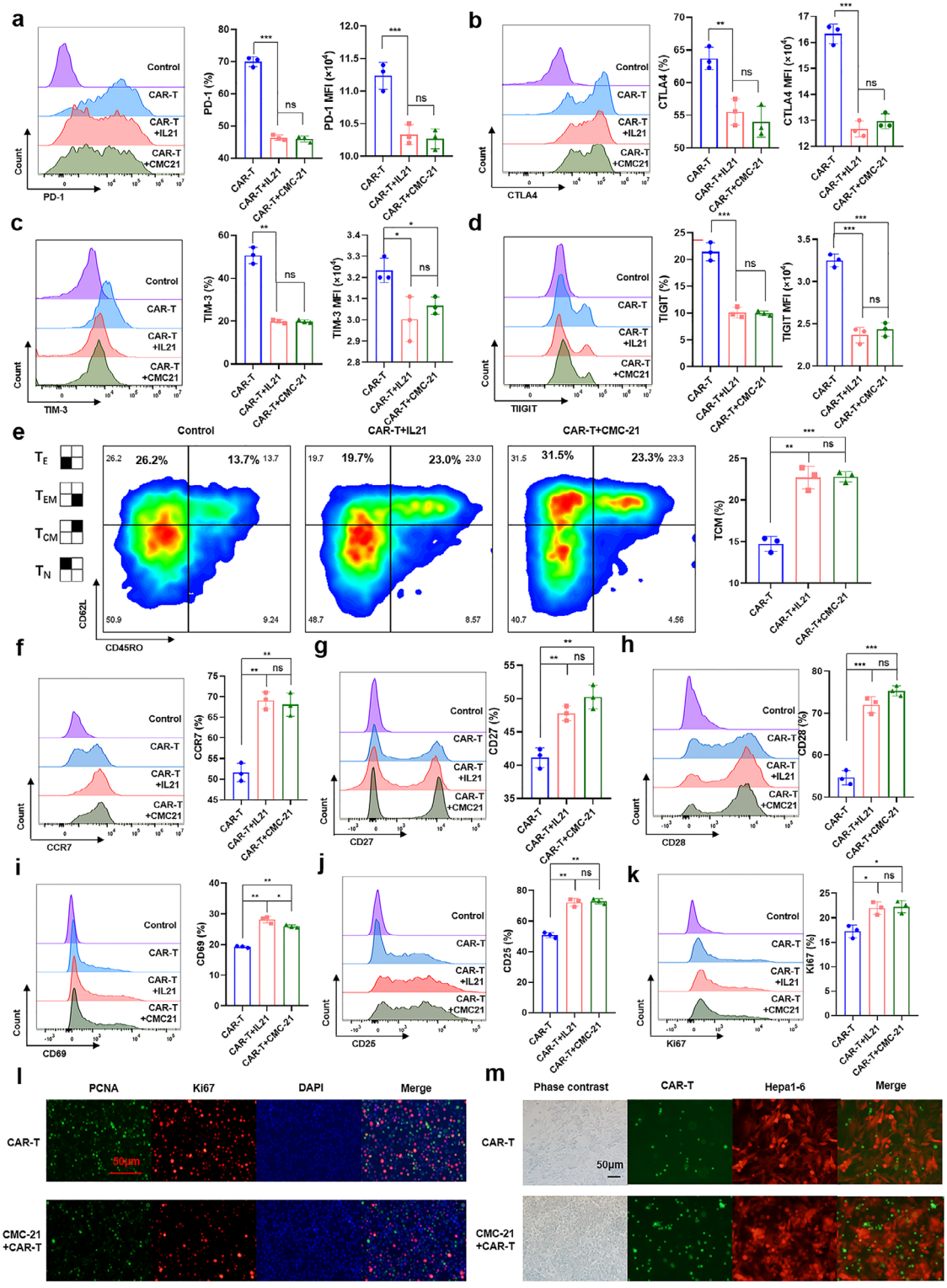

Figure 8. CMC-21 NPs improved CAR-T cells with a superior phenotype. The expression of immune checkpoints PD-1 a), CTLA4 b), TIM-3 c), and TIGIT d) of GPC3 CAR-T cells incubated with IL-21 or CMC-21 NPs were assayed. e) The TCM compartment of human CAR-T cells, with a $CD45RO^{+}$ $CD62L^{+}$ phenotype, was assayed using flow cytometry. Flow cytometry was performed to detect expression of memory marker CCR7 f), low-differentiation associated costimulatory molecules CD27 g), CD28 h), and CD69 i), and proliferation-associated markers CD25 j) and ki67 k) on GPC3 CAR-T cells stimulated with IL-21 or CMC-21 NPs. l) Immunofluorescence imaging of tumor sections stained with PCNA (green), ki67 (red), DAPI (blue). m) The transwell assay. Magnification: ×400. (Scale bar, 50 μm). Data presented are the mean±SD of three separate experiments. ns means no significant difference, $^{*}p < 0.05$, $^{**}p < 0.01$, $^{***}p < 0.001$ compared with indicated group.

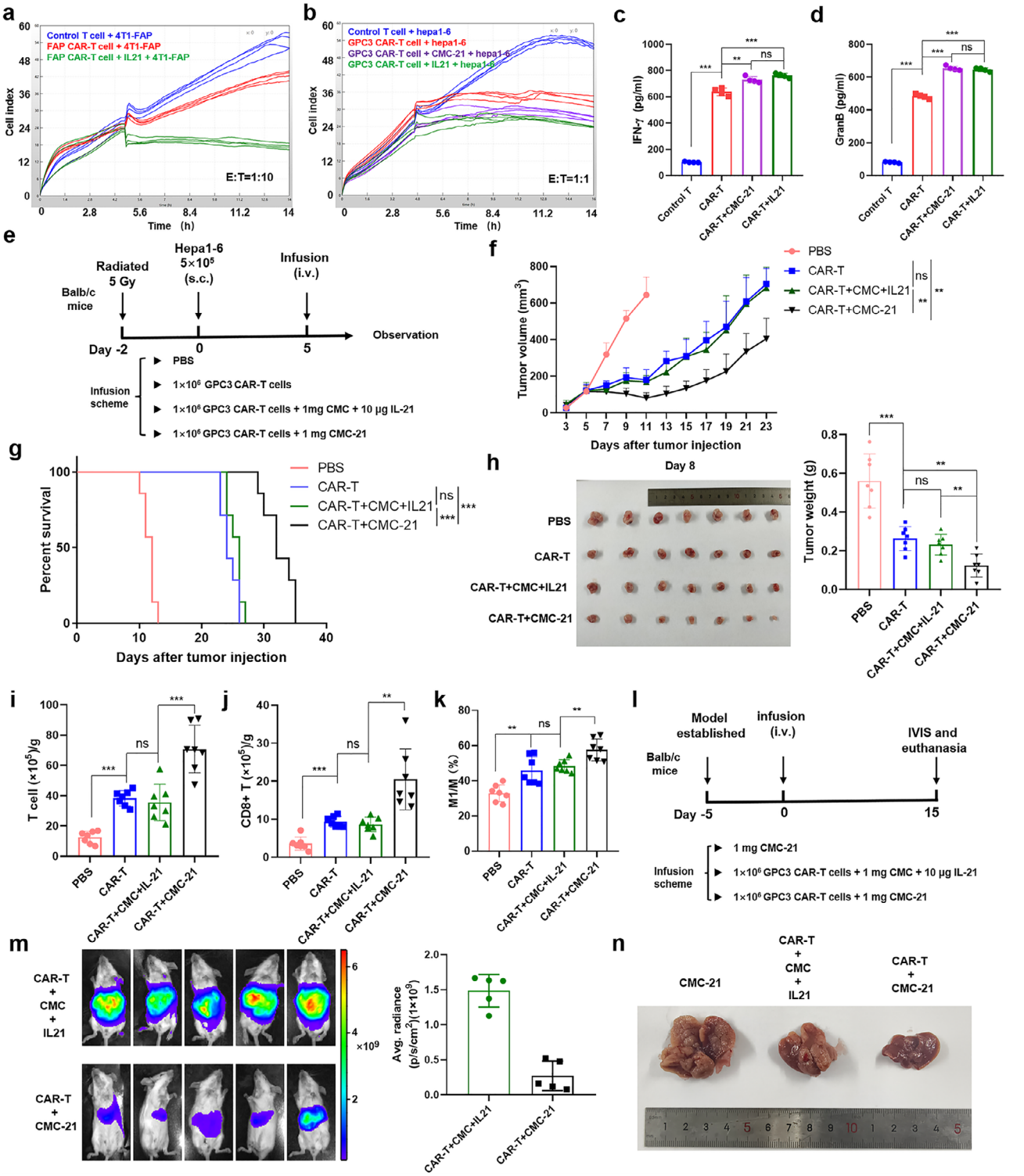

Figure 9. The IL-21 released gradually enhanced antitumor activity of CAR-T cells. a) The cytotoxicity curve of FAP CAR-T cells with or without IL-21. b) The cytotoxicity curve of GPC3 CAR-T cells to hepa1-6 cells with IL-21 or CMC-21 NPs. The levels of IFN-γ c) and granzyme B d) in supernatant released from GPC3 CAR-T cells against hepa1-6 cells were detected. e) Experimental design. f) Tumor size was measured once every 2 days. g) Survival curve of tumor-bearing mice and statistical analysis was performed using the log-rank (Mantel–Cox) test. h) Images of tumor-bearing mice and tumor weight ($n = 7$). Intrinsic T cells i), $CD8^+$ T cells j), and M1-like macrophages k) in tumor tissues were assayed. l) Therapeutic experimental design of liver orthotopic tumor-bearing mouse model. m) Tumor burden was determined by bioluminescent imaging (BLI) ($n = 5$ mice per group). n) Macroscopic morphologies of dissected liver tissues in orthotopic liver tumor-bearing mice on the 15th day of different treatments. Data presented are the mean±SD of three separate experiments. ns means no significant difference, $^*p < 0.05$, $^{**}p < 0.01$, $^{***}p < 0.001$ compared with indicated group.

ment, liver tumors in mice treated with CAR-T cell + CMC + IL-21 developed rapidly, while GPC3 CAR-T cells + CMC-21 NPs clearly controlled HCC growth (Figure 9l). Similar macroscopic morphologies were observed in isolated livers (Figure 9m), indicating the excellent antitumor effects of GPC3 CAR-T cell + CMC-21 and the advantages of the sustained and gradual release of IL-21 from the CMC nanoplatform.

Gradual and sustained IL-21 released from the CMC nanoplatform effectively activated CAR-T cells and intrinsic immune cells; thus, antitumor activity was obviously enhanced when the TME was improved by CMC.

3. Conclusion

In summary, we developed a tumor-targeting immunotherapeutic nanoformulation by integrating CAR-T cells with a CMC-21 vitality backpack. As a proof of concept, we selected CMC NPs for their dual capability to oxygenate the TME through H_2O_2 catalysis while simultaneously neutralizing tumor acidity. Furthermore, CMC NPs promoted tumor cell death through mitochondrial homeostasis regulation. Their porous structure facilitated high-efficiency IL-21 loading, which enhanced CAR-T cell functionality and activated endogenous immune cells. The in vitro and in vivo results showed that the combination treatment of CAR-T cells and CMC-21 possesses great potential for antitumor immune activation based on the gradual release of IL-21 through efficient TME remodeling and sustained CAR-T cell immune activation. This innovative immune cell-nanomaterial conjugation strategy represents both a breakthrough in CAR-T cell therapy for solid tumors and a platform technology with broad clinical potential. However, certain limitations remain, including uncharacterized CAR-T cell persistence and potential long-term effects of CMC NPs in vivo that require further investigation. In the future, studies of CAR-T cells combined with CMC NPs for the treatment of a variety of solid and hematological tumors should be performed.

4. Experimental Section

Synthesis of $CaMnCO_3$ and $CaMnCO_3$-IL-21 NPs: Calcium chloride, Manganese (II) chloride, anhydrous sodium carbonate, polyacrylic acid (PAA, Mw = 2000), and 1-(3-dimethylaminopropyl)-3-ethylcarbodiimide hydrochloride (EDC) were bought from Shanghai Macklin Biochemical Co., Ltd.

The $CaMnCO_3$ NPs were synthesized by the following method. 0.111 g $CaCl_2$, 0.08g $MnCl_2{\cdot}4H_2O$ and 0.16 g PAA were adequately dissolved in 10 mL H_2O, 0.15 g Na_2CO_3 was also dissolved in 10 mL H_2O. The Na_2CO_3 aqueous was slowly added to the ionic solution under stir conditions. After the reaction for 60 min, the white product was obtained and further collected by dialysis. The $CaMnCO_3$-IL-21 NPs were synthesized by absorbing 2 mL $CaMnCO_3$ (2mg mL^{-1}) with 20 µg IL-21 (10 wt.%).

The CMC-IL-21 NPs were conjugated on the surface of CAR-T cells through the following method. 2 mL CMC-IL-21 (2mg mL^{-1}) NPs were added with 1 mM EDC for 30 min, and then purified with centrifugation. The treated CMC-IL-21 NPs at the designed concentration were further added to the CAR-T cell suspension to endow the conjugation between the cells surface and NPs.

Characterization: The morphology and element distribution characterization of nanomaterials were obtained from transmission electron microscopy (TEM) and high-resolution transmission electron microscopy (HRTEM) (JEM-2100, JEOL, Japan) respectively. The morphology and element distribution of cells were characterized by scanning electron microscope (SEM, S-4800, Hitachi, Japan). The material structure information was analyzed by X-ray diffraction (XRD, D8 Advance, Bruker, Germany). The functional group information was analyzed by Fourier transform infrared spectra (FTIR, Nicolet Nexus 670, Thermo Fisher Scientific). The element valence and composition were analyzed by x-ray photoelectron spectroscopy (XPS, ESCALAB 250, ThermoFisher). The zeta potential value and size distribution of nanomaterials were analyzed by the dynamic light scattering analyzer (ZetaPALS, Brookhaven Instrument Crop). The UV–vis-light absorption spectra were analyzed by UV—vis spectrophotometer (UV-6100, Meipuda, China).

Cellular Culture: The following cell lines were cultured in DMEM (Gibco): HEK293T, NIH3T3, 4T1, and Hepa1-6 cells. Mouse B cell lymphoma cell line A20 was cultured in RPMI 1640 medium (Gibco). Mouse T cells were cultured in RPMI 1640 medium supplemented with 50 IU ml^{-1} interleukin-7 (IL-7), 50 IU ml^{-1} interleukin-15 (IL-15), 10% fetal bovine serum (Gibco), 2 mM L-glutamine, 100 U ml^{-1} penicillin and 100 µg ml^{-1} streptomycin. DMEM media were supplemented with 10% fetal bovine serum (Gibco), 2 mM L-glutamine, 100 U ml^{-1} penicillin and 100 µg ml^{-1} streptomycin. All cells were cultured at 37 °C in a humidified 5% CO_2-containing atmosphere. All cell lines were from the American Type Culture Collection (Manassas, VA).

Mouse CAR Vector Construction and CAR-T Cell Production: CARs specific for mouse FAP and GPC3 were synthesized by Han Bio. (Shanghai, China), as described below. Briefly, the cassette encoding the single-chain antibody targeting FAP or GPC3, CD8 transmembrane domain, 41BB endodomain, and CD3ζ-chain of the T cell receptor complex were cloned into the pLVX-EF1a-IRES-Puro to generate the lentiviral vector.

To generate mouse CAR-T cells, C57BL/6J mice were euthanized and the spleen was isolated, then, the spleen was ground, and mononuclear cells were isolated by density gradient centrifugation using Ficoll-Paque (GE Healthcare), and T cells were obtained using sorting kit (Stemcell). T cells were stimulated with CD3/CD28 activation beads (Miltenyi Biotec) at a 1:1 ratio (T cell: bead) for 48 h in RPMI1640 medium supplemented with 50 IU mL^{-1} IL-7 and 50 IU mL^{-1} IL-15. After stimulating for 48 h, activated T cells were transduced with lentiviruses (MOI = 50) (Hanbio Tech, Shanghai, China) and NewHelix Biotech). Then, 15 h later, T cells were harvested and cultured with RPMI1640 medium with IL-7 and IL-15.

Flow Cytometry: The phenotype of primary cells and cell lines was determined using the following antimouse antibodies: CD45-PerCP/Cyanine 7 (Biolegend, 103113), CD45-PerCP/Cyanine 5.5 (Biolegend, 103132), CD3-APC (Biolegend, 100236), CD3-PE (Biolegend, 100205), NK1.1-FITC (Biolegend, 156508), F4/80-APC (Biolegend, 123122), CD11b-FITC (Biolegend, 101205), CD86-APC (Biolegend, 374207), CD4-PerCP/Cyanine 7 (Biolegend, 100421), CD8-PerCP/Cyanine 5.5 (Biolegend, 100733), CD206-PE (eBioscience, 12-2061-80), His-FITC (Biolegend, 362618), TIM-3-APC (Biolegend, 134007), CTLA4-PerCP/Cyanine 5.5 (Biolegend, 106315), PD-1-PerCP/Cyanine 7 (Biolegend, 109109), TIGIT-APC (Biolegend, 142105), CD62L-PE (Biolegend, 980710), CCR7-APC (Biolegend, 120107), CD27-PerCP/Cyanine 7 (Biolegend, 124215), CD28-APC (Biolegend, 122016), CD25-APC (Biolegend, 162105), CD69-PerCP/Cyanine 5.5 (Biolegend, 104521), Ki67-APC (Biolegend, 652405) and CD45RO-PE (Biolegend, 304210). $CD45^+$ $CD11b^+$ $F4/80^+$ $CD206^-$ cells were defined as M1 and $CD45^+$ $CD11b^+$ $F4/80^+$ $CD206^+$ cells were defined M2 macrophages. The cell viability was assayed using Annexin V-APC/PI Apoptotic Kit (Multi Sciences) according to the manufacturer's instructions. All cells were collected and incubated with antibodies at room temperature for 20–25 min, washed three times with PBS, and analyzed using a flow cytometer (Cytoflex, Beckman Coultre). Then, all samples were analyzed using FlowJo software (V.10.1, TreeStar) and GraphPad Prism Software V.6.01.

Enzyme-linked Immunosorbent Assay (ELISA): The supernatants were collected and the mouse cytokines IFN-γ and Granzyme B were measured using the corresponding ELISA kits (Multi Sciences) following the manufacturer's instructions. The results represented the mean ± SD of three separate experiments.

Cytotoxicity Assay: To validate the killing specificity of the constructed CAR-T cells, mouse FAP antigen expression constructs were transformed into cells for use in subsequent experiments. The In vitro antitarget

cytotoxicity of mouse CAR-T cells was determined at E:T using a Smart cell real-time monitor (East China University of Science and Technology, Shanghai, six broad beans; CM100-α). The cell index was correlated with the number of cells attached to the bottom of the plate. Briefly, ten thousand target cells were seeded into 96-well plates. ≈ 5 h later, ten thousand CAR-T or control T cells were added to plates and co-cultured overnight. Then the growth curve of target cells was monitored using a Smart cell real-time monitor.

The CCK8 Assay: The hepa1-6 and NIH3T3 cells treated with different dose of CMC NPs were placed in 96-well plates at a density of 5000 cells per well. CCK8 (KeyGen BioTECH, CN) detection solution (10 µL) was added to each well. After allowing the reaction to proceed for 1 h, the absorbance of each group was measured at 450 nm using a microplate reader. Detection was performed at 0, 24, 48, and 72 h after cell plating.

RNA-Seq Analysis: The GPC3 CAR-T cells were cocultured with or without 5 µg ml^{-1} CMC NPs. 12 h later, CMC NPs were removed. 24 h later, total RNA of CAR-T cells was extracted from CAR-T cells, and messenger RNA libraries were prepared using RNA simple Total RNA Kit (DP419, TIANGEN). Paired-end libraries were synthesized using U-mRNAseq Library Prep Kit (AT4221, KAITAI-BIO) with Ribo off rRNA Depletion Kit (N407, Vazyme), and the output SAM files were converted to binary alignment/map files and sorted using SAM tools (V.1.3.1).

Western Blotting: Whole-cell lysates of cells were generated the proteins were transferred onto PVDF membranes. The following primary antibodies were used: anti-CD3ζ (BD Biosciences), anti-Bcl-XL (Cell Signaling Technology, 2764), anti-BCL-2 (Cell Signaling Technology, 3498), anti-caspase-3 (Cell Signaling Technology, 9661), anti-HIF-1α (Proteintech, 20960-1-AP), anti-Ki67 (Proteintech, 84432-1-RR), anti-TFAM (Proteintech, 22586-1-AP), anti-TOM20 (Proteintech, 11802-1-AP) and anti-actin (Proteintech, 60008-1-Ig). After blocking, the blots were waved at 4 °C with the primary antibodies, followed by incubation with secondary antibodies (Solarbio) at RT. Images were captured using a visualizer (Tanon 4600). Image processing was carried out using the Image J software.

H&E Staining: Hematoxylin and eosin staining was performed on tumors isolated from mice. The tumors were surgically excised from euthanized mice and fixed using formalin. And then, tissues were dehydrated, embedded in paraffin, sectioned, and dewaxed. The slides were dyed using H&E staining and observed under a fluorescence microscope.

Immunofluorescence Staining: Paraffinized sections or paraformaldehyde fixed cells were rehydrated, and antigens were retrieved in an EDTA buffer. Samples were blocked for 30 min with 3% goat serum and 0.2% Bovine Serum Albumin in PBS, followed by first and double immunostaining. Nuclei were stained with DAPI and mounted with an antifade solution. The sections were photographed with an LSM980 laser scanning confocal microscope (Carl ZEISS AG, Oberkochen Germany). The images were quantified according to the positive area per field using Image J 1.45 software (National Institutes of Health, Bethesda, USA).

Seahorse Assay: The seahorse assay was performed to measure the oxygen consumption rate (OCR) of hepa1-6 cells. Briefly, hepa1-6 cell with different CMC concentrations were seeded in a Seahorse culture plate (Seahorse Bioscience, North Billerica, MA, USA) at 37 °C for 40 min. OCR was measured using an XF96 Seahorse Extracellular Flux Analyzer (Agilent Technologies, Santa Clara, CA, USA) following the manufacturer's instructions.

ROS Measurement: ROS in hepa1-6 and 4T1 cells were detected using ROS Assay Kit (Beyotime) and pH was measured using BCECF AM Kit (Beyotime) according to the manufacturer's instructions using flow cytometry. And ROS deletion experiment was performed using ROS inhibitor ROS-IN-2 (MedChemExpress, HY-149586) or 200 µM NMN (Beyotime) according to the manufacturer's instructions.

Measurement of Mitochondrial Membrane Potential ($\Delta\Psi m$): To measure the $\Delta\Psi m$ of hepa1-6 cells, the fluorescent probe JC-1 (5,5',6,6'-tetrachloro-1,1',3,3'-tetraethylbenzimi-dazolylcarbocyanine iodide) (Beyotime, C2006) was used according to the manufacturer's protocol. JC-1 exists as a monomer at low values of $\Delta\Psi m$ (green fluorescence), and forms aggregates at high $\Delta\Psi m$ (red fluorescence). Mitochondrial depolarization was indicated by a decrease in the polymer:monomer fluorescence intensity ratio. JC-1 staining was observed and photographed under a fluorescence microscope.

Transwell Assay: 5×10^5 hepa1-6-mCherry cells were added to the basolateral chamber of a 5.0 µm pore size transwell apparatus (Corning). 2×10^5 CAR-T cells dyed with fluorescent stain-CFSE were loaded in the upper chamber in serum-free X-VIVO15 media. After 12 h of co-culture, images of the basolateral chamber were acquired using the inverted fluorescence microscope (ZEISS HAL 100, Carl Zeiss AG).

MR Imaging (Magnetic Resonance Imaging): For T1-weight MR imaging, the tumor-bearing **mice** were intravenously injected with 1 mg CMC NPs suspension per mouse or combined with 1×10^6 FAP CAR-T cells. And 8 h later, MR imaging was implemented by a 1.5 T MR imaging instrument.

In Vivo Bioluminescence Imaging: D-luciferin (Beyotime) in PBS (1.5 mg mL^{-1}) was used as a substrate for spontaneous HCC following the manufacturer's protocols. Tumor progression was monitored by bioluminescence imaging using an IVIS Spectrum Imaging System (PerkinElmer). Living Image 4.5.5 (PerkinElmer) was used to acquire (and later quantify) the data 10 min after intraperitoneal injection of D-luciferin into animals that were anesthetized with 150 mg kg^{-1} of 1% pentobarbital sodium (Sigma–Aldrich). Imaging settings were kept the same throughout the entire time course of an experiment.

Animal Experiments: All animal studies were conducted in line with protocols approved by the Institutional Animal Care and Use Committee of Shandong University. Experiments were conducted in the Animal Experiment Center of Shandong University (Accreditation number: ECSBMSSDU2019-2-78) under specific pathogen-free conditions. The female Balb/c mice with an average weight of 16–18 g were purchased from Beijing Vital River Laboratory Animal Technology Co., Ltd. After irradiation with 5 Gy, the mice were subcutaneously injected with FAP-overexpressing tumor cells or hepa1-6 cells in the right flank. Treatment commenced when the tumor reached 50 or 100 mm^3. The mice were randomly allocated to four groups, with seven mice in each group: i) the group injected with PBS during each treatment; ii) the group injected with CMC-21 NPs (100 µL) during each treatment; iii) the group injected with CAR-T cells during each treatment; iv) the group injected with CAR-T cells plus CMC-21 NPs during each treatment. The tumor size of each mouse was measured every two days. The following formula was used to calculate tumor size: $4\pi/3\times(\text{tumor length}/2)\times(\text{tumor width}/2)^2$. The mice were euthanized in a humane manner when death was imminent or when the tumor size reached ≈10 mm. To detect loading efficiency, 1 mg CMC and 100 µg IL-21 were thoroughly mixed in 2 mL water. One hour later, the CMC NPs were discarded by centrifugation and the residual IL-21 was analyzed using ELISA. This concentration was 90% of the original concentration (loading rate of ≈10:1).

To establish a *Myc*-induced spontaneous HCC model, 12 µg vector pT3-AKT-Fluc, 12 µg oncogene c-*Myc*-expressing vector pT3-EF1a-c-myc, and 1.36 µg transposase-encoding plasmid pCMV(CAT)T7-SB100 per mouse were dissolved in 1 mL 0.9% saline solution, and then were hydrodynamically injected into the lateral tail vein in < 10 s per injection. HCC progression was monitored by bioluminescence imaging using an IVIS Spectrum system.

Statistical Analysis: The in vitro experiments were repeated at least three times for each group, and a one-way analysis of variance or Student's *t*-test was used to compare quantitative data (mean ± SD) between the samples. A p-value < 0.05 indicated significance. For in vivo experiments, the survival curves of mice were generated using the Kaplan–Meier method, and survival data were analyzed using the log-rank (Mantel–Cox) test. Statistical significance was set at $p < 0.05$. Statistical analyses were performed using GraphPad Prism (GraphPad Software, La Jolla, CA, USA).

Supporting Information

Supporting Information is available from the Wiley Online Library or from the author.

Acknowledgements

B.W., Y.X., and Y.J. contributed equally to this work. This work was supported by the Natural Science Foundation of Shandong Province (ZR2023QC179, ZR2023QE146, ZR2022MH281, ZR2021QH276, ZR2021QH074, ZR2020QH265), the National Natural Science Foundation of China (82302067, 82370618, 82160124, 82100641, 82203658).

Conflict of Interest

The authors declare no conflict of interest.

Author Contributions

B.H.W., Y.C.X., and Y.J. performed the experiments, acquired and interpreted the data, and wrote the manuscript. Y.Y.D., D.J.L., and M.H.S. were involved in the construction of plasmid and lentiviral vectors. H.D. and X.Y.W. contributed to the flow cytometry. Y.N.S. participated in immunofluorescent staining and graphic plotting. H.M.L. and J.N.Q. contributed to the animal studies partly. S.B.Z., Q.Z., and J.Z.D. designed the project, assisted in the experiments, provided funding support, and finalized the manuscript.

Data Availability Statement

The data that support the findings of this study are openly available in Repository name at https://doi.org/10.1002/adfm.202213921, reference number 8.

Keywords

CAR-T cell, hepatocellular carcinoma, immunoactivation, tumor microenvironment, vitality backpacks

Received: February 8, 2025
Revised: April 18, 2025
Published online: May 9, 2025

[1] R. C. Sterner, R. M. Sterner, *Blood Cancer J.* **2021**, *11*, 69.
[2] Y. Liu, Z. Xun, K. Ma, S. Liang, X. Li, S. Zhou, L. Sun, Y. Liu, Y. Du, X. Guo, T. Cui, H. Zhou, J. Wang, D. Yin, R. Song, S. Zhang, W. Cai, F. Meng, H. Guo, B. Zhang, D. Yang, R. Bao, Q. Hu, J. Wang, Y. Ye, L. Liu, *J. Hepatol.* **2023**, *78*, 770.
[3] S. Das, J. Valton, P. Duchateau, L. Poirot, *Front. Immunol.* **2023**, *14*, 1172681.
[4] G. G. Demissie, Y.-C. Chen, S.-Y. Ciou, S.-H. Hsu, C.-Y. Wang, C.-C. Huang, H.-T. Chang, Y.-C. Lee, J.-Y. Chang, *J. Colloid Interface Sci.* **2025**, *685*, 396.
[5] G. Getachew, C. Korupalli, A. Rasal, J. Y. Chang, *Compos. Part B: Eng.* **2021**, *226*, 109364.
[6] A. E. Ringel, J. M. Drijvers, G. J. Baker, A. Catozzi, J. C. García-Cañaveras, B. M. Gassaway, B. C. Miller, V. R. Juneja, T. H. Nguyen, S. Joshi, C.-H. Yao, H. Yoon, P. T. Sage, M. W. LaFleur, J. D. Trombley, C. A. Jacobson, Z. Maliga, S. P. Gygi, P. K. Sorger, J. D. Rabinowitz, A. H. Sharpe, M. C. Haigis, *Cell* **2020**, *183*, 1848.
[7] B. Cao, M. Liu, L. Wang, K. Zhu, M. Cai, X. Chen, Y. Feng, S. Yang, S. Fu, C. Zhi, X. Ye, J. Zhang, Z. Zhang, X. Yang, M. Zhao, Q. Wu, L. Xu, L. Yang, H. Lian, Q. Zhao, Z. Zhang, *Nat. Commun.* **2022**, *13*, 6203.
[8] D. Kolb, N. Kolishetti, B. Surnar, S. Sarkar, S. Guin, A. S. Shah, S. Dhar, *ACS Nano* **2020**, *14*, 11055.
[9] T. Fang, X. Cao, L. Wang, M. Chen, Y. Deng, G. Chen, *Bioact. Mater.* **2024**, *32*, 530.
[10] J. Li, W. Li, K. Huang, Y. Zhang, G. Kupfer, Q. Zhao, *J. Hematol. Oncol.* **2018**, *11*, 1.
[11] M. R. Davis, Z. Zhu, D. M. Hansen, Q. Bai, Y. Fang, *Cancer Lett.* **2015**, *358*, 107.
[12] S. H. A. Eivary, R. K. Kheder, S. K. Najmaldin, N. Kheradmand, S.-A. Esmaeili, J. Hajavi, *Med. Onc.* **2023**, *40*, 191.
[13] S. Deng, Z. Sun, J. Qiao, Y. Liang, L. Liu, C. Dong, A. Shen, Y. Wang, H. Tang, Y.-X. Fu, H. Peng, *JCI Insight* **2020**, *5*, 132000.
[14] Y. Shi, T. Lammers, *Acc. Chem. Res.* **2019**, *52*, 1543.
[15] W. Nawaz, S. Xu, Y. Li, B. Huang, X. Wu, Z. Wu, *Acta Biomater.* **2020**, *109*, 21.
[16] G. Luo, X. Li, J. Lin, G. Ge, J. Fang, W. Song, G. G. Xiao, B. Zhang, X. Peng, Y. Duo, B. Z. Tang, *ACS Nano* **2023**, *17*, 15449.
[17] M. Fang, J. Zheng, J. Wang, C. Zheng, X. Leng, E. Wen, P. Li, H. Ran, L. Zhang, Z. Wang, *Biomater. Res.* **2024**, *28*, 0028.
[18] W. B. Direrse, G. Getachew, A. Wibrianto, A. S. Rasal, V. S. Gurav, M. Zakki Fahmi, J.-Y. Chang, *J. Colloid Interface Sci.* **2023**, *647*, 528.
[19] C. Korupalli, C.-C. Kuo, G. Getachew, W. B. Direrse, A. Wibrianto, A. S. Rasal, J.-Y. Chang, *J. Colloid Interface Sci.* **2023**, *643*, 373.
[20] J. Duan, S. Zhao, Y. Duan, D. Sun, G. Zhang, D. Yu, Y. Lou, H. Liu, S. Yang, X. Liang, C. Ma, H. Liu, J. Qiu, L. Gao, Y. Sang, *Adv. Healthcare Mater.* **2024**, *13*, 2303963.
[21] L. Lybaert, K. A. Ryu, L. Nuhn, R. De Rycke, O. De Wever, A. C. Chon, A. P. Esser-Kahn, B. G. De Geest, *Chem. Mater.* **2017**, *29*, 4209.
[22] Z. Dong, L. Feng, Y. Hao, M. Chen, M. Gao, Y. Chao, H. Zhao, W. Zhu, J. Liu, C. Liang, Q. Zhang, Z. Liu, *J. Am. Chem. Soc.* **2018**, *140*, 2165.
[23] R. Bagur, G. Hajnóczky, *Mol. Cell* **2017**, *66*, 780.
[24] F. Kong, H. You, K. Zheng, R. Tang, C. Zheng, *Int. J. Biol. Macromol.* **2021**, *192*, 745.
[25] L. Zheng, Y. Ding, S. Fang, W. Yang, J. Chen, J. Ma, M. Wang, J. Wang, F. Zhang, X. Guo, K. Zhang, G.-F. Shu, Q. Weng, F. Wu, Z. Zhao, M. Chen, J. Jiansong, *ACS Nano* **2024**, *18*, 27597.
[26] A. Alaimo, M. Lorenzoni, P. Ambrosino, A. Bertossi, A. Bisio, A. Macchia, E. Zoni, S. Genovesi, F. Cambuli, V. Foletto, D. De Felice, M. V. Soldovieri, I. Mosca, F. Gandolfi, M. Brunelli, G. Petris, A. Cereseto, A. Villarroel, G. Thalmann, F. G. Carbone, M. Kruithof-de Julio, M. Barbareschi, A. Romanel, M. Taglialatela, A. Lunardi, *Cell Death Dis.* **2020**, *11*, 1039.
[27] P. Zheng, B. Ding, Z. Jiang, W. Xu, G. Li, J. Ding, X. Chen, *Nano Lett.* **2021**, *21*, 2088.
[28] J. An, K. Zhang, B. Wang, S. Wu, Y. Wang, H. Zhang, Z. Zhang, J. Liu, J. Shi, *ACS Nano* **2020**, *14*, 7639.
[29] X. Deng, T. Liu, Y. Zhu, J. Chen, Z. Song, Z. Shi, H. Chen, *Bioact. Mater.* **2024**, *33*, 483.
[30] J. Asin-Cayuela, C. M. Gustafsson, *Trends Biochem. Sci.* **2007**, *32*, 111.
[31] B. Lu, J. Lee, X. Nie, M. Li, Y. I. Morozov, S. Venkatesh, D. F. Bogenhagen, D. Temiakov, C. K. Suzuki, *Mol. Cell* **2013**, *49*, 121.
[32] R. Di Maio, P. J. Barrett, E. K. Hoffman, C. W. Barrett, A. Zharikov, A. Borah, X. Hu, J. McCoy, C. T. Chu, E. A. Burton, T. G. Hastings, J. T. Greenamyre, *Sci. Transl. Med.* **2016**, *8*, 342ra78.
[33] X. Guo, S. Tan, T. Wang, R. Sun, S. Li, P. Tian, M. Li, Y. Wang, Y. Zhang, Y. Yan, Z. Dong, L. Yan, X. Yue, Z. Wu, C. Li, K. Yamagata, L. Gao, C. Ma, T. Li, X. Liang, *Hepatology* **2023**, *78*, 468.
[34] T. D. Tlsty, P. W. Hein, *Curr. Opin. Genet. Dev.* **2001**, *11*, 54.
[35] L.-L. Lu, S.-x. Xiao, Z.-y. Lin, J.-j. Bai, W. Li, Z.-q. Song, Y.-h. Zhou, B. Lu, W.-Z. Wu, *Cell Biol. Toxicol.* **2023**, *39*, 3101.
[36] T. Patra, D. M. Cunningham, K. Meyer, K. Toth, R. B. Ray, A. Heczey, R. Ray, *Mol. Ther.* **2023**, *31*, 715.
[37] L. Xia, Q. Teng, Q. Chen, F. Zhang, *Int. J. Nanomed.* **2020**, *15*, 2197.
[38] L. Zhou, Y. Li, D. Zheng, Y. Zheng, Y. Cui, L. Qin, Z. Tang, D. Peng, Q. Wu, Y. Long, Y. Yao, N. Wong, J. Lau, P. Li, *Mol. Ther.: Onc.* **2024**, *32*, 200817.

[39] Z. Yin, Q. Ji, D. Wu, Z. Li, M. Fan, H. Zhang, X. Zhao, A. Wu, L. Cheng, L. Zeng, *ACS Appl. Mater. Interfaces* **2021**, *13*, 14928.
[40] M. A. Amini, A. Z. Abbasi, P. Cai, H. Lip, C. R. Gordijo, J. Li, B. Chen, L. Zhang, A. M. Rauth, X. Y. Wu, *JNCI: J. Natl. Cancer Inst.* **2019**, *111*, 399.
[41] C. Wang, Z. Dong, Y. Hao, Y. Zhu, J. Ni, Q. Li, B. Liu, Y. Han, Z. Yang, J. Wan, K. Yang, Z. Liu, L. Feng, *Adv. Mater.* **2021**, *34*, 2106520.
[42] D. L. Porter, B. L. Levine, M. Kalos, A. Bagg, C. H. June, *N. Engl. J. Med.* **2011**, *365*, 725.
[43] E. Goulmy, *Immunol. Rev.* **1997**, *157*, 125.
[44] Y. Luo, Z. Chen, M. Sun, B. Li, F. Pan, A. Ma, J. Liao, T. Yin, X. Tang, G. Huang, B. Zhang, H. Pan, M. Zheng, L. Cai, *Biomaterials* **2022**, *281*, 121341.
[45] N. Pozzesi, S. Gizzi, F. Gori, C. Vacca, L. Cannarile, C. Riccardi, D. V. Delfino, *J. Chemother.* **2007**, *19*, 562.
[46] P. Berraondo, I. Etxeberria, M. Ponz-Sarvise, I. Melero, *Clin. Cancer Res.* **2018**, *24*, 2716.
[47] A. H. Long, W. M. Haso, J. F. Shern, K. M. Wanhainen, M. Murgai, M. Ingaramo, J. P. Smith, A. J. Walker, M. E. Kohler, V. R. Venkateshwara, R. N. Kaplan, G. H. Patterson, T. J. Fry, R. J. Orentas, C. L. Mackall, *Nat. Med.* **2015**, *21*, 581.
[48] M. Xiao, Q. Tang, S. Zeng, Q. Yang, X. Yang, X. Tong, G. Zhu, L. Lei, S. Li, *Biomater. Res.* **2023**, *27*, 47.
[49] M. Li, F. Chen, Q. Yang, Q. Tang, Z. Xiao, X. Tong, Y. Zhang, L. Lei, S. Li, *Biomater. Res.* **2024**, *28*, 0023.
[50] S. Zhao, C. Wang, P. Lu, Y. Lou, H. Liu, T. Wang, S. Yang, Z. Bao, L. Han, X. Liang, C. Ma, L. Gao, *J. Immuno Ther. Cancer* **2021**, *9*, 003176.
[51] D. Wang, B. Aguilar, R. Starr, D. Alizadeh, A. Brito, A. Sarkissian, J. R. Ostberg, S. J. Forman, C. E. Brown, *JCI Insight* **2018**, *3*, 99048.

